Available online at www.sciencedirect.com
ScienceDirect
Geochimica et Cosmochimica Acta 73 (2009) 6065–6083
Geochimica et Cosmochimica Acta
www.elsevier.com/locate/gca

Comparative dissolution kinetics of biogenic and chemogenic uraninite under oxidizing conditions in the presence of carbonate

Kai-Uwe Ulrich [a,*], Eugene S. Ilton [b], Harish Veeramani [c], Jonathan O. Sharp [c,1], Rizlan Bernier-Latmani [c], Eleanor J. Schofield [d,2], John R. Bargar [d], Daniel E. Giammar [a]

[a] Department of Energy, Environmental and Chemical Engineering, Washington University, One Brookings Drive, St. Louis, MO 63130, USA
[b] Pacific Northwest National Laboratory, 902 Battelle Blvd, Richland, WA 99352, USA
[c] Ecole Polytechnique Fédérale de Lausanne, CH-1015 Lausanne, Switzerland
[d] Stanford Synchrotron Radiation Lightsource, 2575 Sand Hill Rd, Menlo Park, CA 94025, USA

Received 8 January 2009; accepted in revised form 9 July 2009; available online 14 July 2009

Abstract

The long-term stability of biogenic uraninite with respect to oxidative dissolution is pivotal to the success of *in situ* bioreduction strategies for the subsurface remediation of uranium legacies. Batch and flow-through dissolution experiments were conducted along with spectroscopic analyses to compare biogenic uraninite nanoparticles obtained from *Shewanella oneidensis* MR-1 and chemogenic $UO_{2.00}$ with respect to their equilibrium solubility, dissolution mechanisms, and dissolution kinetics in water of varied oxygen and carbonate concentrations. Both materials exhibited a similar intrinsic solubility of $\sim 10^{-8}$ M under reducing conditions. The two materials had comparable dissolution rates under anoxic as well as oxidizing conditions, consistent with structural bulk homology of biogenic and stoichiometric uraninite. Carbonate reversibly promoted uraninite dissolution under both moderately oxidizing and reducing conditions, and the biogenic material yielded higher surface area-normalized dissolution rates than the chemogenic. This difference is in accordance with the higher proportion of U(V) detected on the biogenic uraninite surface by means of X-ray photoelectron spectroscopy. Reasonable sources of a stable U(V)-bearing intermediate phase are discussed. The observed increase of the dissolution rates can be explained by carbonate complexation of U(V) facilitating the detachment of U(V) from the uraninite surface. The fraction of surface-associated U(VI) increased with dissolved oxygen concentration. Simultaneously, X-ray absorption spectra showed conversion of the bulk from $UO_{2.0}$ to UO_{2+x}. In equilibrium with air, combined spectroscopic results support the formation of a near-surface layer of approximate composition $UO_{2.25}$ (U_4O_9) coated by an outer layer of U(VI). This result is in accordance with flow-through dissolution experiments that indicate control of the dissolution rate of surface-oxidized uraninite by the solubility of metaschoepite under the tested conditions. Although U(V) has been observed in electrochemical studies on the dissolution of spent nuclear fuel, this is the first investigation that demonstrates the formation of a stable U(V) intermediate phase on the surface of submicron-sized uraninite particles suspended in aqueous solutions.

1. INTRODUCTION

The anthropogenic use of uranium (U) for nuclear fuel production, weapons manufacturing and research has resulted in widespread contamination of soils and groundwater. One of the most stable natural forms of uranium is uraninite, a hyperstoichiometric mineral in the range of UO_{2+x} ($0 < x < 0.25$) that ubiquitously contains impurities

* Corresponding author. Present address: BGD Soil and Groundwater Laboratory GmbH, Tiergartenstrasse 48, D-01219 Dresden, Germany. Fax: +49 351 438 99 039.
E-mail address: kulrich@bgd-gmbh.de (K.-U. Ulrich).
[1] Present address: Colorado School of Mines, Environmental Science & Engineering Division, Golden, CO.
[2] Present address: The University of Kent, School of Physical Sciences, Canterbury, Kent, UK.

0016-7037/$ - see front matter © 2009 Elsevier Ltd. All rights reserved.
doi:10.1016/j.gca.2009.07.012

when present in rock or sediment formations (Finch and Ewing, 1992; Janeczek and Ewing, 1992a,b). Because several species of metal and sulfate reducing bacteria are known to mediate the reduction of dissolved U(VI) to U(IV) (Suzuki and Suko, 2006; Wall and Krumholz, 2006), the engineered stimulation of microbial growth in contaminated media by providing an electron donating carbon source (e.g., ethanol, acetate, lactate, glucose) has been proposed to initiate the precipitation of sparingly soluble uraninite (Gorby and Lovley, 1992; Lovley and Phillips, 1992; Lovley et al., 1991). This strategy of *in situ* bioremediation has been studied for more than a decade (N'Guessan et al., 2008; Renshaw et al., 2007 and references therein). Uranium immobilization can only be successful if dissolution rates of biogenic uraninite and the likelihood of reoxidation are low. Although the structure of biogenically immobilized uranium has not yet been fully characterized in field-scale U(VI) bioreduction experiments, nanoparticulate UO_{2+x} obtained from cell cultures is better understood and typically exhibits a composition close to $UO_{2.0}$ (Burgos et al., 2008; Schofield et al., 2008; Singer et al., 2007, 2009). Hence, even more knowledge is required with respect to the chemical stability of biogenic UO_{2+x}, in particular the kinetics of dissolution reactions under environmentally relevant scenarios. In this paper, the term "bio-UO_2" is used for biogenic uraninite prepared in the absence of dopants, irrespective of the actual stoichiometry (the number of x in UO_{2+x}). Unless otherwise specified, the term "syn-UO_2" is used for chemogenic UO_{2+x} where the stoichiometry may range between $0 \leqslant x \leqslant 0.33$ dependent on the chemical conditions present and the degree of surface oxidation.

In natural groundwater, the potential of the U(IV)/U(VI) redox couple is expected to range between −42 and +86 mV, depending on a number of parameters including the pH and concentrations of Ca^{2+} and dissolved inorganic carbon (DIC) (Brooks et al., 2003; Wall and Krumholz, 2006). Some of the most potent electron acceptors for U(IV) oxidation are dissolved oxygen, nitrate, nitrite, and solid Mn(IV) and Fe(III). The processes of biogenic uraninite reoxidation and its suppression have been investigated for lab-grown cultures and sediments amended with a carbon source *in situ* or in flow-through columns. Dissolved oxygen (DO) is one of the strongest oxidants of U(IV), and it has been reported to oxidize bioreduced U(IV) within several hours to days in stirred batch experiments (half-life of $\leqslant$1 h) (Gu et al., 2005; Zhou and Gu, 2005) or when mixed with bioreduced sediment (Zhong et al., 2005). However, continuous-flow-through dissolution studies using bioreduced sediments in soil columns demonstrated that nitrate and not DO can be the dominant oxidant of U(IV) in sediments. The authors hypothesized that oxygen was scavenged more rapidly by other reduced compounds or by microbial metabolism (Moon et al., 2007). In addition to nitrate, which is often found in U-contaminated sites (Finneran et al., 2002), intermediate products of dissimilatory nitrate reduction or denitrification such as NO_2^-, N_2O and NO can oxidize and remobilize U(IV) (Senko et al., 2002).

Mn oxides can rapidly oxidize bio-UO_2 in the absence of biological activity (Fredrickson et al., 2002), and freshly formed biogenic MnO_2 can be an even more effective oxidant for UO_{2+x} than DO under low partial pressure (P_{O2}) conditions (Chinni et al., 2008). Ferrihydrite can rapidly oxidize bio-UO_2, generating dissolved U(VI) and Fe^{2+}. The oxidation rate is affected by the aqueous speciation of U(VI) which is a function of pH, carbonate, and Ca^{2+} concentrations because those ions tend to form stable ternary complexes with U(VI) lowering the free energy of uraninite oxidation (Ginder-Vogel et al., 2006). Reactive Fe(III) oxyhydroxide can also result from enzymatic Fe(II) oxidation coupled to nitrate reduction, or from Fe(II) oxidation with nitrite (Senko et al., 2005a). Other work found that humic substances, siderophores, and (bi)carbonate from the degradation of organics can increase the rate of bio-UO_2 oxidation by formation of stable U(VI) complexes (Frazier et al., 2005; Gu et al., 2005; Wan et al., 2005).

The stability of bio-UO_2 can be enhanced by preventing reoxidation of U(IV), for example when sulfides such as mackinawite (FeS) or decaying biomass are present and act as oxygen-scavenging redox buffers or when sulfite is added to the system (Abdelouas et al., 1999; Wu et al., 2007). Another strategy for stabilizing bio-UO_2 is to keep the rate of U(VI) bioreduction low, which may give rise to larger and more aggregated particles that are more resistant to oxidation (Senko et al., 2007). In batch experiments with air-equilibrated water, small particles of bio-UO_2 were oxidized much faster than were larger particles and aggregates. However, the U(VI) bioreduction rate is not a unique tool to control particle size. This has been exemplified for *Shewanella oneidensis* MR-1 for which the bioreduction rate did not affect particle size in contrast to results from *Shewanella putrefaciens* CN32 (Burgos et al., 2008).

In most of the above-mentioned studies, the generated U(IV) phase has not been structurally characterized and there is little robust information regarding the stability of the solid phase. Although several authors have applied X-ray absorption near-edge spectroscopy (XANES) to quantify the proportion of biogenic U(IV) and U(VI) in their systems, structural characterization of the U(IV) mineral phase is lacking in most U bioreduction - reoxidation studies (Ginder-Vogel et al., 2006; Senko et al., 2005b; Wan et al., 2005; Wu et al., 2007; Zhong et al., 2005). The combination of structural investigations with studies on dissolution kinetics is important because structural differences are expected to modulate chemical stability. For example, Finch and Ewing (1992) reported that cations incorporated in the uraninite lattice and a corrosion rind of U(VI) on the mineral surface inhibited further U(IV) oxidation. This made uraninite stable at redox conditions under which synthetic UO_2 corrodes.

Recent research shows that the nano-sized UO_{2+x} material generated by lab-grown cultures of *S. oneidensis* MR-1 is near-stoichiometric ($x < 0.05$) and structurally similar to chemogenic $UO_{2.00}$ (Schofield et al., 2008). A comparison of both types of material with respect to stability under reducing, carbonate-free conditions showed that dissolution rates had the same order of magnitude when normalized to surface area (Ulrich et al., 2008). The objective of the present study is to investigate the effects of carbonate and dissolved oxygen on the stability of biogenic and

chemogenic UO_{2+x}. Dissolution rates are presented as a function of varied DO and DIC concentrations, and a conceptual mechanistic model of possible surface reactions supported by spectroscopic results is discussed. The ultimate goal of this research is to predict the long-term stability of a structurally well-characterized biogenic uraninite under chemical conditions relevant to contaminated groundwater.

2. EXPERIMENTAL SECTION

2.1. Materials

Reagents of certified ACS grade or better and ultrapure water (resistivity >18.5 MΩ cm) were used. The UO_{2+x} materials were prepared in an anaerobic chamber (Coy Laboratory Products) as described in Ulrich et al. (2008). Biogenic UO_{2+x} was produced by the facultative anaerobic *S. oneidensis* strain MR-1. Bacteria of the genus *Shewanella* have been found in the subsurface, e.g., at the Hanford site (Fredrickson et al., 2007). U(VI) reduction was carried out in the presence of 1.2 mM uranyl acetate, 30 mM $NaHCO_3$, and 20 mM lactic acid at pH 6.3 and 8.0, giving rise to different ratios of $UO_2(CO_3)_2^{2-}$ and $UO_2(CO_3)_3^{4-}$ as the dominant U(VI) species under these conditions. The yield of U(IV) oxide was close to or above 99% at both pH conditions. The products are referred to as bio6-UO_2 and bio8-UO_2. Upon completion of U(VI) bioreduction, the mixture of bio-UO_2 and cells was treated overnight with 1 M NaOH. The organic debris was removed from UO_2 by phase separation employing anaerobic hexane. Subsequent treatment with 0.1 M $NaHCO_3$ solution and repeated washing with ultrapure anaerobic water removed less than 1% of the total uranium, presumably U(VI). The cleaned bio-UO_2 solids were stored anaerobically in light-protected serum bottles until being used in dissolution experiments.

Synthetic uraninite (syn-UO_2) was prepared by reduction of studtite ($UO_2O_2{\cdot}4H_2O_{(s)}$) at 400 °C for 4 h in a stainless steel reactor in presence of $H_{2(g)}$ (Eq. (1)).

$$UO_2O_2 \cdot 4H_2O_{(s)} + 2H_{2(g)} \rightarrow UO_{2(s)} + 6H_2O \quad (1)$$

Studtite was precipitated by mixing ~88 mM H_2O_2 (Sigma Aldrich) with 2.5 mM UO_2Cl_2 (Eq. (2)).

$$UO_2Cl_2 + H_2O_2 + 4H_2O \rightarrow UO_2O_2 \cdot 4H_2O_{(s)} + 2HCl \quad (2)$$

A light yellow precipitate settled within 3 days. It was dialyzed against ultrapure water, dried, and identified as pure $UO_2O_2{\cdot}4H_2O_{(s)}$ by X-ray diffraction (XRD). The UO_2Cl_2 stock solution was prepared by heating $UO_2(NO_3)_2{\cdot}6H_2O$ (Antec, Inc.) at 275 °C for 3 days to produce solid UO_3 that was then dissolved in 0.5 M HCl (trace metal grade, Fisher Scientific).

2.2. Structural properties of unreacted UO_{2+x}

The biogenic and synthetic materials differed notably in their particle size and surface area. The bio-UO_2 particles exhibited a nano-scale size range of 1.5–3.5 nm (Schofield et al., 2008) and an average specific surface area of 50.1 m^2/g obtained from multipoint N_2-BET. This surface area is lower than expected for a spherical UO_2 particle of that size (150–360 m^2/g), and it is lower than recently published N_2-BET data of biogenic UO_2 obtained from *S. putrefaciens* CN32 (93–129 m^2/g, Singer et al., 2009), suggesting significant agglomeration of the nanoparticles. Because particle agglomeration could not be prevented over the course of dissolution experiments, the obtained dissolution rates were normalized to the measured rather than the calculated surface area. The mean diameter of the syn-UO_2 particles was two orders of magnitude larger (100–200 nm) and revealed a matching N_2-BET surface area of 5.9 m^2/g.

X-ray absorption spectroscopy and synchrotron based X-ray powder diffraction results showed that the structures of the bio6-UO_2 and bio8-UO_2 materials were similar, suggesting particles with a highly ordered core in which the U-lattice is preserved (stoichiometry close to $UO_{2.00}$, $x < 0.05$) and an outer region with local disorder (Schofield et al., 2008; Ulrich et al., 2008). The lattice parameter of the uncleaned bio-UO_2 was similar to that of chemogenic $UO_{2.00}$, suggesting that the surface energy is not sufficient to strain the intermediate- and long-range structure of the bio-UO_2 particles. Hence, similar intrinsic thermodynamic and kinetic properties would be expected.

2.3. Dissolution experiments

Dissolution rates were quantified using magnetically-stirred continuous-flow tank reactors (CFR, volume of 12.6 mL) operated in the dark at room temperature (20 ± 1 °C) as described in detail elsewhere (Ulrich et al., 2008). Each reactor was loaded with a weighed amount of syn-UO_2 powder or a defined aliquot of well-mixed bio-UO_2 suspension with known UO_2 concentration and fed with equilibrated solutions of given chemical composition. All feed solutions contained 1 or 5 mM HEPES buffer adjusted to pH 7.5 or 8.0. $NaHCO_3$ was added to obtain DIC concentrations of 0.1, 1.0, or 10 mM. Customized gas mixtures were purged into the feed solution to maintain reducing conditions (95% N_2 + 5% H_2 in presence of a Pd catalyst) or oxidizing conditions with 1 vol% O_2 (balance N_2) or 21 vol% O_2 (compressed air). Influent flow rates were set between 1.0 and 2.1 mL/min and gravimetrically monitored based on the effluent volume collected in test tubes using an automatic fraction collector. The DO concentration of the influent was monitored with a flow-through DO probe (Microelectrodes, Inc.) installed in the tubing between the feed reservoir and the CFR.

Because the available amount of biogenic UO_2 was limited, the CFR experiments were carried out either in a consecutive or intermittent treatment mode. In the consecutive mode, different feed solutions were pumped through the CFR for about 40 residence times for each solution in a sequence of increasing P_{O2} (0, 1, 21 vol% while maintaining 1 mM DIC), or increasing concentration of carbonate (0, 0.1, 1.0, 10 mM while maintaining P_{O2} constant at 1 vol%). Both series started with anoxic atmosphere using DIC-free, HEPES-buffered feed solution. The same condition was applied during the first and third treatment steps of the intermittent dissolution modes, interrupted by either

feeding 1 mM DIC under reducing conditions or providing DO equilibrated to a 1% P_{O2} headspace.

Equilibrium $[U]_{diss}$ of UO_2 under reducing conditions was determined by switching the operation mode from flow-through (i.e., CFR) to stirred batch reactor (SBR). By operating in this order, any labile U(VI) species present with the initial solid were washed away during the CFR mode prior to starting the equilibrium measurement in the SBR mode. The SBR experiments were performed in a closed system in the glovebox. Samples for U analysis were collected at several points in elapsed time using a needle syringe and filtered through aluminum oxide filter units (Anotop10, Whatman, Inc.) with 0.02 μm pore size. For spectroscopic investigations, the residual solids of the suspension were either accumulated on a filter membrane or centrifuged. The wet paste was loaded into an aluminum sample holder with Kapton windows and stored at anoxic conditions until the analysis by X-ray absorption spectroscopy. For X-ray photoelectron spectroscopy, the wet samples were dried in an anaerobic chamber prior to the analysis.

2.4. Analysis

The pH was periodically measured in the feed solution and the effluent samples. Effluent samples selected for total U analysis were acidified to 0.1 M nitric acid prior to measurement by ICP-MS (Agilent 7500ce). The ICP-MS method for uranium had a detection limit <10 ng/L. Several samples were also analyzed specifically for U(VI) using a kinetic phosphorescence analyzer (KPA) (Chemchek, Richland, WA, USA) with a detection limit of <0.1 μg/L (Chinni et al., 2008).

X-ray absorption spectroscopy (XAS) and high-resolution X-ray photoelectron spectroscopy (XPS) were used to determine the redox state and stoichiometry of uranium in the bulk and near the surface of UO_{2+x} particles before and after their reaction in dissolution experiments.

2.4.1. X-ray photoelectron spectroscopy

The XPS analyses were carried out at Lehigh University using a Scienta ESCA300. The instrument's operational parameters as well as methodologies for coping with potential artifacts are discussed elsewhere (Ilton et al., 2004). Briefly, an intense monochromatic Al Kα X-ray beam, which is generated with a rotating anode, was used. Operational conditions yielded Fermi edge widths of 0.41–0.31 eV for Ag^0, depending on the pass energy used. Regional scans of the U4*f* region were recorded and the energy scale was referenced to adventitious C1s at 285.0 eV. For a number of samples, and in particular for the uncleaned biogenic UO_2 samples, the C1s structure was complicated. In such cases, the C1s peak was curve-resolved with a sufficient number of Gaussians to obtain a good fit. The lowest energy Gaussian was then set as the energy scale reference.

Standards for U(VI), U(V) and U(IV) were used to determine satellite structures and primary peak parameters. Schoepite was precipitated from a supersaturated solution and used as a U(VI) standard. A U(V)–U(VI) oxyhydroxide phase provided the standard for U(V). The synthesis and characterization of this compound has been described in detail in previous work (Belai et al., 2008). The U(V) component was derived by fitting the mixed valence phase with the U(VI) component (obtained from schoepite) and solving for the U(V) component. The U(IV) standard was prepared as described in Section 2.1 and characterized as stoichiometric $UO_{2.00}$ by X-ray powder diffraction and XAS (Ulrich et al., 2008).

Spectra were best fit by non-linear least squares using the CasaXPS curve resolution software. A Shirley background was extended from about 8 eV below the $4f_{7/2}$ peak to about 20 eV above the $4f_{5/2}$ peak. This binding energy (BE) spread encompassed the major satellite features. The BE and intensity of individual components, which included satellites and primary peaks, were allowed to move as a packet relative to the other components (i.e., satellite-primary peak BE separations and relative intensities were fixed for a given component). A single, but variable full-width-at-half-maximum (FWHM) value was used for all the core peak components. Satellite and core peak FWHMs were set at a fixed ratio for each component. The outstanding energy resolution obtained by the Scienta300, combined with tightly correlating core peaks to their corresponding satellites, imposed severe constraints on the solution for each sample.

Prior to XPS analyses, the wet samples were dried and stored in an airtight container for 24–48 h. The container was then placed in an Ar filled glove bag attached to the entry port of the X-ray photoelectron instrument such that the sample transfer occurred with minimal exposure to oxygen. Sequential analyses were taken on the same spot, for each specimen, in order to check for beam induced reduction. The sequential spectra for the U(IV) standard indicated no change, and the U(V) standard was stable over the first several spectra in the sequence. However, most other specimens, including the U(VI) standard, did indicate reduction over time. Fortunately, reduction was systematic and slow. In order to minimize the reduction of our U(VI) standard, it was analyzed at a lower photon flux. The XPS spectra presented in this work are always the first in each sequence. Tabulated data give both the valence state derived from the first spectrum in the sequence and a value obtained by extrapolating to time zero.

2.4.2. X-ray absorption spectroscopy

X-ray absorption near-edge (XANES) and extended X-ray absorption fine structure (EXAFS) spectroscopy was carried out at SSRL beamlines 11–2 and 10–2 using a Si (2 2 0) double-crystal monochromator. Spectra across the U L_3 electron binding energy edge position were collected in transmission mode. Unreacted cleaned biogenic samples were analyzed in a liquid nitrogen cryostat (77 K) to improve definition of higher-order shells. Reacted samples (subjected to oxidation in the CFRs) were collected on membrane filters which were analyzed at room temperature. The monochromator was calibrated using an yttrium foil. EXAFS spectra were background-subtracted, splined and analyzed using SIXPack (Webb, 2005). Backscattering phase and amplitude functions required for fitting of spectra were obtained from FEFF 8 (Rehr et al., 1992). The

uncertainty of the U-oxidation state by XANES spectroscopy is about 10% for mixtures containing U(IV) and U(VI), based on Singer et al. (2009) and taking into account the lack of knowledge regarding the precise U(VI) species for surface-reacted uraninite.

2.5. Dissolution rate calculation

Dissolution rates of the biogenic and chemogenic UO_2 materials are derived from the mass balance approach (Eq. (3)) described in Ulrich et al. (2008).

$$V \cdot \frac{d[U]_{eff}}{dt} = Q \cdot [U]_{in} - Q \cdot [U]_{eff} + V \cdot R_d \quad (3)$$

In Eq. (3) $[U]_{eff}$ and $[U]_{in}$ (mol L^{-1}) are the U concentrations in the effluent and influent, V (L) is the reactor volume, Q (L min^{-1}) is the flow rate, and R_d (mol L^{-1} min^{-1}) is the rate of U release to solution from UO_2 dissolution. Given a constant R_d and ideal flow conditions, it takes about five residence times, $\tau = VQ^{-1}$ (min), to achieve steady-state, i.e., $\frac{d[U]_{eff}}{dt} = 0$. Assuming $[U]_{in}$ is zero, the dissolution rate can be calculated:

$$R_m = \frac{Q \cdot [U]_{ss}}{V \cdot [solid]} \quad (4)$$

$$R_n = \frac{Q \cdot [U]_{ss}}{V \cdot SSA \cdot [solid]} \quad (5)$$

where R_m (mol g^{-1} min^{-1}) and R_n (mol m^{-2} min^{-1}) are the dissolution rates normalized to mass and specific surface area, SSA (m^2 g^{-1}), respectively, $[U]_{ss}$ (mol/L) is the effluent uranium concentration at steady-state, and $[solid]$ (g L^{-1}) is the mass concentration of UO_2 in the reactor. The rate calculation accounts for the changes in $[solid]$ and SSA with time, resulting from UO_2 dissolution (for details see Ulrich et al., 2008).

To calculate the reaction rate constant, the Gibbs free energy of reaction needs to be considered (Kraemer and Hering, 1997; Lasaga et al., 1994). While the goal was to run the dissolution experiments far from equilibrium, a linear rate law function (Eq. (6)) has been used to account for the distance to equilibrium, where IAP is the ion activity product, and K_{sp} the solubility product with respect to UO_2 dissolution under anoxic conditions (Eq. (7)) and with respect to metaschoepite ($UO_3 \cdot 2H_2O$) under oxidizing conditions (Eq. (8)). For the anoxic conditions, the measured equilibrium concentration of dissolved uranium, $[U]_{eq}$, has been used. The predicted $[U]_{eq}$ of metaschoepite was calculated as a function of $[U]_{diss}$, pH, and [DIC] using MINEQL+ (Schecher and McAvoy, 1998) and a $\log K_{sp}$ of 5.39 for the dissolution reaction (Eq. (8)) as suggested by Jang et al. (2006) and Langmuir (1978). The dissolution rate constant k (mol m^{-2} min^{-1}) for these reactions can then be calculated from Eq. (9).

$$f(\Delta G) = \left(1 - \frac{IAP}{K_{sp}}\right) \quad (6)$$

$$UO_{2(s)} + 4H^+ \rightarrow U^{4+} + 2H_2O \quad (7)$$

$$UO_3 \cdot 2H_2O_{(s)} + 2H^+ \rightarrow UO_2{}^{2+} + 3H_2O \quad (8)$$

$$R_n = k \cdot \left(1 - \frac{IAP}{K_{sp}}\right) = k \cdot \left(1 - \frac{[U]_{ss}}{[U]_{eq}}\right) \quad (9)$$

3. RESULTS

3.1. Oxidative UO_2 dissolution

To study the effects of DO on the stability of bio-UO_2 and syn-UO_2 in aqueous systems, oxygen-free conditions provide the lowest dissolution rates and were applied as the first step of consecutive UO_{2+x} dissolution (Ulrich et al., 2008). In anoxic, carbonate-free water at pH 7.5 ± 0.2, the dissolved U concentrations in the effluent reached steady-state well below or close to the predicted equilibrium solubility of amorphous $UO_{2(am)}$ of 3.2×10^{-9} M based on the NEA thermodynamic database (Guillaumont et al., 2003). The calculated dissolution rates of both bio- and chemogenic materials were within the same order of magnitude when normalized to surface area, which is consistent with their structural homology (Ulrich et al., 2008). Under reducing conditions, U(VI) was undetectable ($<4.2 \times 10^{-10}$ M) in the effluent as verified by KPA. This result suggests that the anoxic UO_2 dissolution was primarily driven by hydrolysis of U(IV) and not by oxidation to U(VI) (Eq. (7)).

Even though carbonate is a common groundwater constituent, its aqueous complexes with U(IV) are very weak (Guillaumont et al., 2003) and thus are not expected to change the solubility and dissolution kinetics of $UO_{2(am)}$ under the experimental conditions. To test this hypothesis, 1 mM DIC was added to the anoxic feed solution as the second step of consecutive UO_2 dissolution. Surprisingly, the effluent $[U]_{diss}$ increased by more than one order of magnitude for the syn-UO_2 (Fig. 1c), and about three orders of magnitude for the bio-UO_2 (Fig. 1a and b). Whereas the effluent of bio8-UO_2 and bio6-UO_2 approached a pseudo steady-state $[U]_{diss}$ between 1 and 5 μM, the effluent $[U]_{diss}$ of syn-UO_2 peaked at 0.05 μM and then continuously diminished toward a steady-state concentration around 0.01 μM (Fig. 1c). Roughly the same value has been determined as the experimental equilibrium concentration in the absence of DIC (Ulrich et al., 2008). The dissolution rates of the bio-UO_2 were up to 20-times higher than those of the syn-UO_2 when normalized to surface area (Table 1). Hence, at least for the bio-UO_2, the presence of carbonate considerably accelerated the dissolution process under reducing conditions, which is likely explained by complexation and detachment of a uranium species other than U(IV). Interestingly, effluent analyses by KPA ruled out the possibility of U(VI) mobilization beyond the detection limit of 4.2×10^{-10} M.

Step three of the flow-through UO_{2+x} dissolution experiment showed a change of rate when switching to moderately oxidizing conditions (1 vol% P_{O2}) while keeping the 1 mM DIC feed solution. The introduced oxygen dissolved quickly in the feed solution up to a level of 0.4–0.6 mg/L (Fig. 1d–f), which is consistent with the expected DO equilibrium in water at 20 °C and 1 bar of gas pressure. The effluent $[U]_{diss}$ of the syn-UO_2 material showed the highest

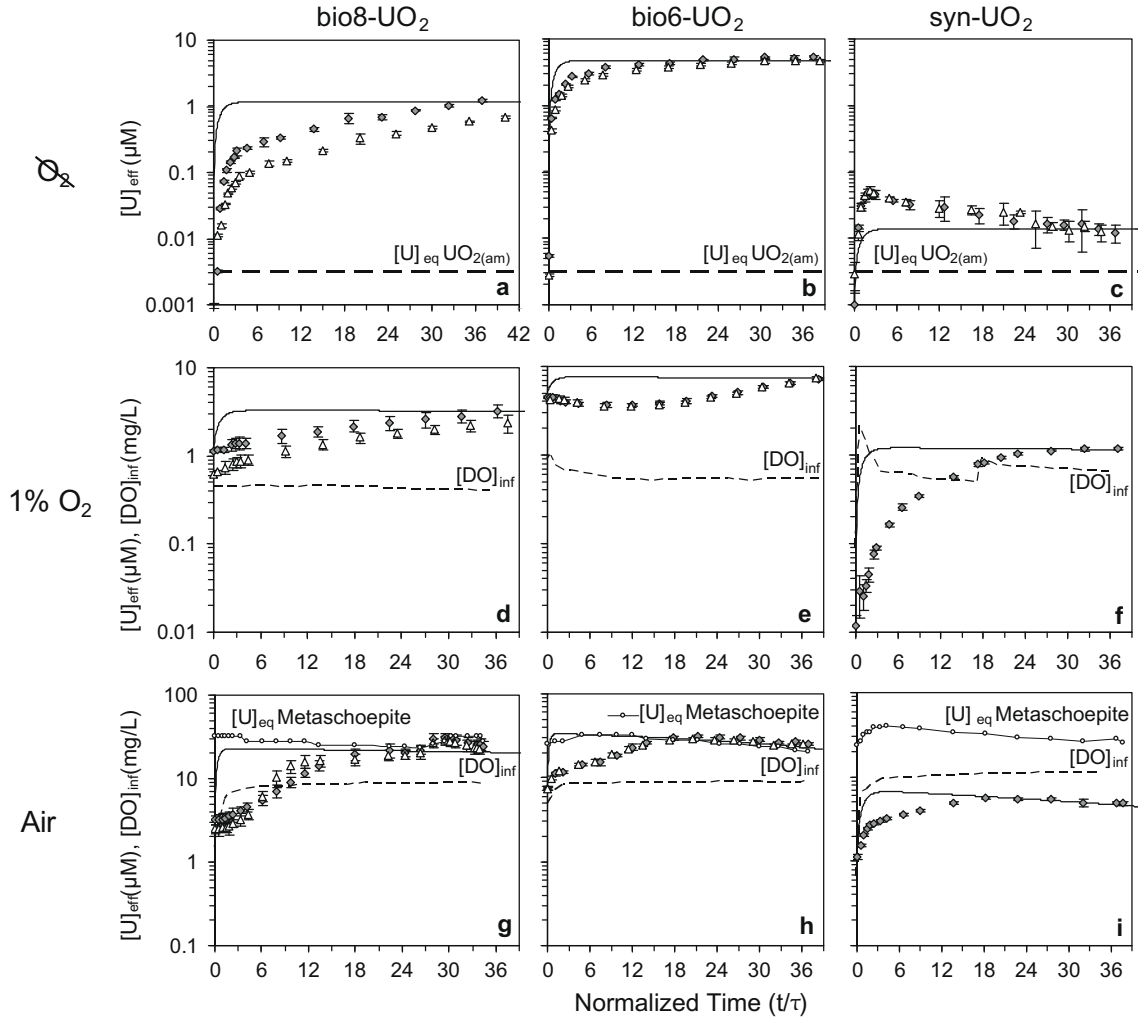

Fig. 1. Flow-through dissolution of bio8-UO_2 (a, d, g), bio6-UO_2 (b, e, h), and syn-UO_2 (c, f, i) as a function of oxygen concentration in the influent, sequentially raised from reducing atmosphere (5 vol% P_{H2}, a–c) to 1 vol% P_{O2} (d–f) to 21 vol% P_{O2} (g–i; each gas balanced with N_2). The feed solution contained 1 mM DIC at 7.6 ± 0.1, effluent pH was 8.2 ± 0.3. Symbols represent effluent concentrations of dissolved U of two replicate reactors as a function of residence times (t/τ, with $\tau = 6$–9 min. Error bars reflecting one standard deviation of analysis are mostly smaller than the symbol size. The thin dashed lines show the concentration of dissolved oxygen (DO) monitored in the influent. The thick dashed and the dotted lines indicate the equilibrium concentrations of amorphous UO_2 (log K_{sp} −1.5) and metaschoepite, $UO_3{\cdot}2H_2O$ (log K_{sp} −5.39) calculated from thermodynamic data. The solid line shows the modeled response to UO_2 dissolution with rate constants given in Table 1. UO_2 dissolution was continued from a flow-through experiment which ran under reducing conditions in the absence of carbonate (see Ulrich et al, 2008).

increase from 0.01 to 1.2 µM, and appeared to reach steady-state (Fig. 1f). In comparison, the increase of the effluent $[U]_{diss}$ of the bio-UO_2 was more moderate and time-delayed, reflecting only a small acceleration of the dissolution rate upon switching from reducing to moderately oxidizing conditions. Effluent samples analyzed by KPA indicated small fractions of dissolved U(VI) on the order of 5–10% of $[U]_{diss}$, demonstrating that at least part of the biogenic UO_2 material was fully oxidized from U(IV) to U(VI). Assuming that the effluent concentrations were at steady-state and the final stage of U-oxidation would be metaschoepite, the surface area-normalized dissolution rates and rate constants (k) for the biogenic and chemogenic UO_2 materials were of the same order of magnitude and within the range of $1–6 \times 10^{-10}$ mol m^{-2} s^{-1} (Table 1). As already mentioned in Section 2.5, the rate constants were calculated from experimentally measured dissolution rates.

Step four of the flow-through UO_2 dissolution tested the change of rate following an increase from a 1% to a 21 vol% P_{O2} atmosphere in the headspace of a 1 mM DIC feed solution. This change in P_{O2} was quickly recorded by the DO probe in the influent, showing 9–10 mg/L as expected (Fig. 1g–i). In response to the higher DO concentration, the proportion of U(VI) in the effluent exceeded 80% of

Table 1
Comparison of UO_2 dissolution rates obtained from flow-through dissolution in 12.6 mL CFRs under different experimental conditions. U dissolution rates are based on mass (R_m) or surface area (R_n) of UO_2 solids assuming steady-state was reached. The rate constant k accounts for the Gibbs free energy function $f(\Delta G)$, calculated with Eq. (9), Section 2.5. All rates account for the time-dependent loss of material during UO_2 dissolution.

Material	[*Solid*] g/L	Flow rate mL/min	P_{O2} bar	[DIC] M	pH –	R_m mol g^{-1} s^{-1}	R_n mol m^{-2} s^{-1}	$f(\Delta G)$ –	k mol m^{-2} s^{-1}	Ref[a]
This work, anoxic conditions										
Bio6-UO_2	1.15	1.42	$<10^{-6}$	10^{-3}	8.57	8.35×10^{-09}	1.64×10^{-10}	0.896	1.83×10^{-10}	
Bio8-UO_2	1.60	2.02	$<10^{-6}$	10^{-3}	8.58	1.52×10^{-09}	3.03×10^{-11}	0.968	3.13×10^{-11}	
Syn-UO_2	0.79	1.97	$<10^{-6}$	10^{-3}	8.64	4.86×10^{-11}	8.56×10^{-12}	0.997	8.58×10^{-12}	
This work, moderately oxidizing conditions										
Bio6-UO_2	1.73	1.87	0.01	0	8.58	6.63×10^{-11}	1.32×10^{-12}	0.836	1.58×10^{-12}	
Syn-UO_2	1.23	1.81	0.01	0	8.51	2.36×10^{-11}	3.98×10^{-12}	0.920	4.33×10^{-12}	
Bio6-UO_2	1.73	2.01	0.01	10^{-4}	8.22	2.30×10^{-09}	4.57×10^{-11}	0.915	5.00×10^{-11}	
Syn-UO_2	1.23	1.89	0.01	10^{-4}	8.20	1.16×10^{-09}	1.95×10^{-10}	0.991	1.97×10^{-10}	
Bio6-UO_2	1.10	1.18	0.01	10^{-3}	8.17	1.19×10^{-08}	2.27×10^{-10}	0.850	2.67×10^{-10}	
Bio6-UO_2	1.66	1.96	0.01	10^{-3}	8.51	1.47×10^{-08}	2.88×10^{-10}	0.844	3.42×10^{-10}	
Bio8-UO_2	1.59	1.96	0.01	10^{-3}	7.90	4.67×10^{-09}	9.25×10^{-11}	0.940	9.83×10^{-11}	
Syn-UO_2	0.79	1.91	0.01	10^{-3}	8.00	3.94×10^{-09}	6.62×10^{-10}	0.993	6.67×10^{-10}	
Syn-UO_2	1.21	1.98	0.01	10^{-3}	8.58	3.35×10^{-09}	5.63×10^{-10}	0.979	5.75×10^{-10}	
Bio6-UO_2	1.23	1.19	0.01	10^{-2}	8.79	2.53×10^{-08}	4.78×10^{-10}	0.989	4.83×10^{-10}	
Syn-UO_2	1.14	1.97	0.01	10^{-2}	8.71	1.50×10^{-09}	2.50×10^{-10}	0.985	2.54×10^{-10}	
This work, strongly oxidizing conditions										
Bio6-UO_2	1.00	1.19	0.21	10^{-3}	8.25	7.43×10^{-08}	$1.02 \cdot 10^{-09}$	0.407	$2.50 \cdot 10^{-09}$	
Bio8-UO_2	1.56	1.78	0.21	10^{-3}	8.10	5.08×10^{-08}	$9.06 \cdot 10^{-10}$	0.604	$1.50 \cdot 10^{-09}$	
Syn-UO_2	0.75	1.95	0.21	10^{-3}	8.00	2.97×10^{-08}	$4.84 \cdot 10^{-09}$	0.908	$5.33 \cdot 10^{-09}$	
Published data, oxidizing conditions										
UO_2 pellets	1.0 g[b]	0.10	0.05	0	8.0		$3.89 \cdot 10^{-12}$			1
UO_2 pellets	1.0 g[b]	0.10	0.05	0	6.5		$4.86 \cdot 10^{-12}$			1
UO_2 pellets		Batch	0.20	0	7.0		$1.06 \cdot 10^{-11}$			2
Syn-$UO_{2(cr)}$		0.004-0.08	0.21	10^{-3}	8.0		$1.00 \cdot 10^{-10}$			3
UO_2 pellets		unknown	0.21	10^{-2}	8.5		$1.60 \cdot 10^{-10}$			4
Syn-UO_2	0.1 g[b]	0.10	0.21	0	8.6		$8.27 \cdot 10^{-12}$			5
Syn-UO_2	0.1 g[b]	0.19	0.21	10^{-2}	8.4		$1.60 \cdot 10^{-10}$			5

[a] References: (1) Casas et al. (1994), (2) Thomas and Till (1984), (3) Pierce et al. (2005), (4) De Pablo et al. (1996), (5) Bruno et al. (1995). Data are from the present work if no reference is given.
[b] A thin film was used in this work.

$[U]_{diss}$. While the steady-state concentration of both biogenic UO_2 materials approached the calculated equilibrium concentration of metaschoepite, the effluent concentration from chemogenic UO_2 dissolution stayed below equilibrium. Nevertheless, the calculated dissolution rate constants normalized to surface area were close to one another, ranging from 1.5 to 5.3×10^{-9} mol m^{-2} s^{-1} (Table 1). Potential explanations for this behavior are discussed below in Section 4.3.

3.2. Effect of carbonate on UO_{2+x} dissolution under moderately oxidizing conditions

The results shown in the previous section demonstrate that carbonate promotes the dissolution of biogenic UO_2 under reducing conditions. Likewise, the dissolution rates are dependent on [DO], an effect which has been studied at a constant concentration of 1 mM DIC. The following experiment investigated the effect of carbonate on UO_2 dissolution under moderately oxidizing conditions. While maintaining a 1 vol% P_{O2} headspace in the feed solution, the [DIC] was raised step-wise from zero to 0.1, 1.0, and 10 mM by adding the equivalent amount of $NaHCO_3$. In Fig. 2, the effluent $[U]_{diss}$ of bio6-UO_2 (Fig. 2a and c) and syn-UO_2 (Fig. 2b and d) are compared for duplicate runs at each condition. In the absence of DIC, the effluent $[U]_{diss}$ steadily increased without reaching a steady-state within ~40 residence times (t/τ). Hence, the dissolution process accelerated with time, and the highest rates recorded from this period amount to 1.3×10^{-12} and 4.0×10^{-12} mol m^{-2} s^{-1} for the biogenic and the chemogenic UO_2, respectively (Table 1). Upon the addition of 0.1 mM DIC, with the exception of one bio-UO_2 replicate, the effluent $[U]_{diss}$ yielded a transient peak and quickly approached a pseudo steady-state concentration of 0.5–0.6 μM for syn-UO_2 and 1.0–1.6 μM for bio-UO_2 (Fig. 2a and b). The surface area-normalized average dissolution rates were 4.6×10^{-11} and 2.0×10^{-10} mol m^{-2} s^{-1} for the biogenic and the chemogenic UO_2, demonstrating a dissolution-promoting effect of carbonate and a higher dissolution rate constant for the chemogenic material.

After increasing the DIC in the feed solution to 1 mM, the effluent $[U]_{diss}$ increased slightly for the chemogenic and considerably for the biogenic UO_2, reaching a steady-

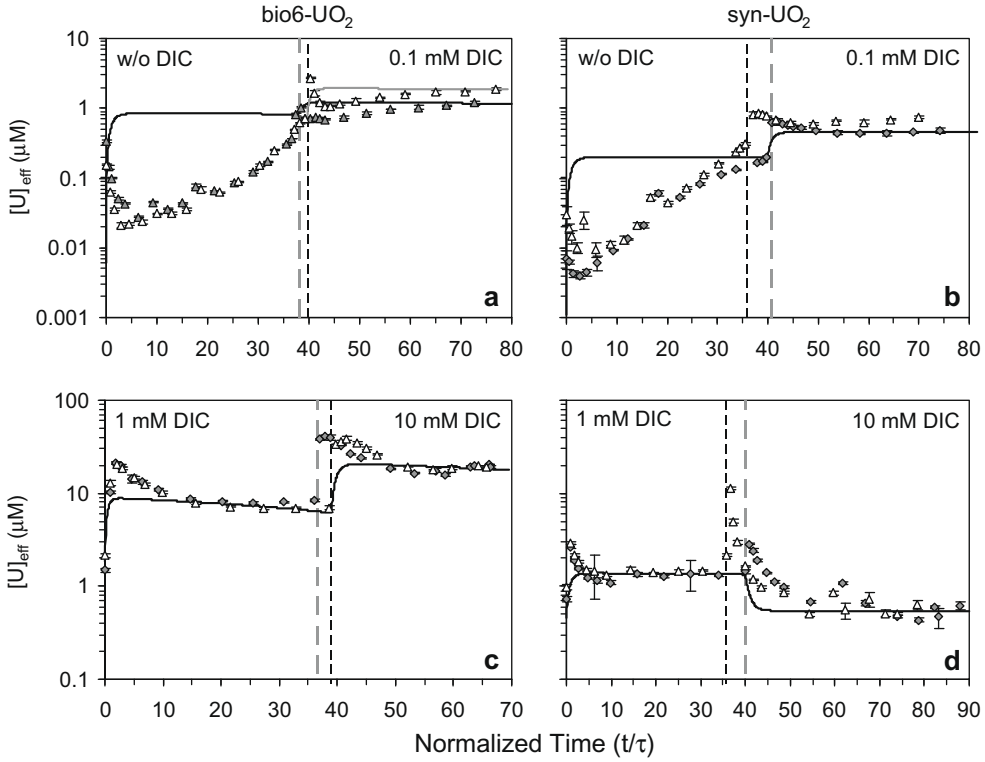

Fig. 2. Flow-through dissolution of bio6-UO_2 (a and c) and syn-UO_2 (b and d) as a function of DIC concentration in the feed solution, sequentially raised from 0 to 0.1 (a and b) and to 1.0 and 10 mM DIC (c and d); vertical dashed lines indicate the switch of experimental conditions for each reactor. The feed solution was equilibrated with 1 vol% P_{O2} and 99 vol% P_{N2}. Symbols represent effluent concentrations of dissolved U of two replicate reactors as a function of residence times (t/τ, with $\tau = 6$–10 min). Error bars reflecting one standard deviation of analysis are mostly smaller than the symbol size. The effluent pH was 8.5 ± 0.4. The solid line shows the modeled response to UO_2 dissolution with rate constants given in Table 1.

state of 1.5 and 7 µM, respectively (Fig. 2c and d). The surface area-normalized dissolution rates yielded 2.9×10^{-10} and 5.6×10^{-10} mol m^{-2} s^{-1} and thus were consistent with the rates determined from the aforementioned dissolution experiment carried out at the same [DIC] and P_{O2} conditions (Table 1). After further increasing the influent [DIC] to 10 mM, the effluent $[U]_{diss}$ of the bio-UO_2 material showed another step-increase and leveled off at a higher steady-state concentration compared to the preceding condition (Fig. 2c). In contrast, for the syn-UO_2 a transient $[U]_{diss}$ peak was followed by a slightly lower steady-state level than during the preceding condition (Fig. 1d). The surface area-normalized dissolution rate constants (k) of the bio- and chemogenic UO_2 were very close to one another, 4.8×10^{-10} and 2.5×10^{-10} mol U m^{-2} s^{-1}, consistent with the structural homology of both materials (see Section 4.3.).

3.3. Effects of intermittent oxygen or carbonate supply on UO_{2+x} dissolution

Both carbonate and DO accelerated the dissolution of the bio- and chemogenic UO_2. To study the reversibility of each dissolution process individually, the syn-UO_2 material was first reacted under carbonate-free reducing conditions and then intermittently treated with either 1 mM DIC or 1 vol% P_{O2} before re-establishing the initial condition. After adding 1 mM DIC, the effluent $[U]_{diss}$ linearly increased indicating that carbonate gradually made the UO_2 surface more susceptible to dissolution (Fig. 3a). If the intrinsic rate of UO_2 dissolution was unaffected by carbonate, the effluent $[U]_{diss}$ would have stayed unchanged as represented by the dashed line. In contrast, an instantaneous increase of the dissolution rate constant would have resulted in a $[U]_{diss}$ curve as shown by the black line. When the influent was switched back to DIC-free water, however, the effluent $[U]_{diss}$ dropped to the preceding concentration level within five residence times, which is consistent with an immediate relapse of the dissolution rate to the preceding value and a washout of excess $[U]_{diss}$ that was consistent with the behavior of a conservative solute in a CFR as demonstrated by the model (black line). This result shows that the promoting effect of carbonate on UO_2 dissolution was fully reversible.

After switching from reducing to oxidizing conditions, provided by a 1 vol% P_{O2} atmosphere in the influent, the effluent $[U]_{diss}$ increased and approached a steady-state of ~1 µM after 14 residence times (Fig. 3b). After reintroducing the anoxic influent, the effluent $[U]_{diss}$ level stayed the same over the subsequent 20 residence times. This result shows that the oxidative dissolution process was not immediately reversible.

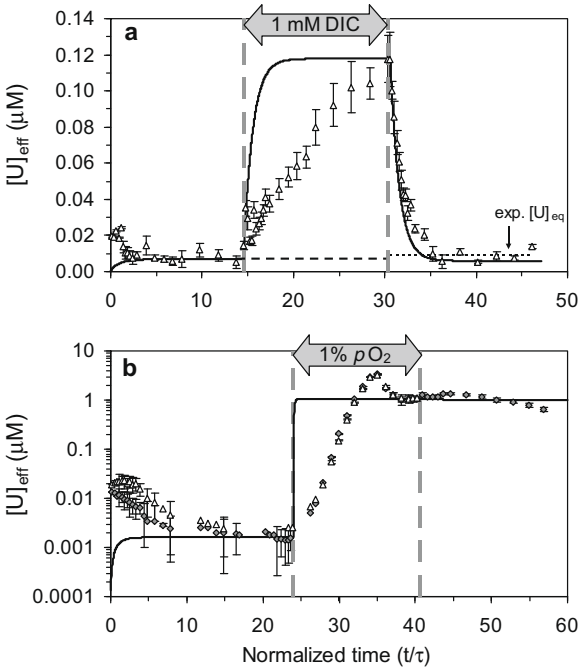

Fig. 3. Effect of intermittent feed of (a) 1 mM DIC, and (b) 1 vol% P_{O2} on the flow-through dissolution of syn-UO_2 at pH 8.0-8.3 (a) and pH~7.5 (b) under otherwise reducing conditions; vertical dashed lines indicate the switch of experimental conditions. Symbols show the effluent concentrations of dissolved uranium as a function of residence times ($\tau = 12$–15 min). Error bars reflecting one standard deviation of analysis are sometimes smaller than the symbol size. The solid line shows the modeled response to a step-function change in UO_2 dissolution with rate constants of (a) 1.3×10^{-11}, 6.3×10^{-11}, and 1.3×10^{-11} mol U m^{-2} s^{-1}, and (b) 4.2×10^{-13} and 1.7×10^{-9} mol U m^{-2} s^{-1}. If carbonate had no effect, $[U]_{eff}$ should follow the dashed steady-state line. The dotted line visualizes the experimentally determined equilibrium concentration.

3.4. XAS and XPS spectroscopic analyses of UO_{2+x}

3.4.1. X-ray absorption spectroscopy

XANES and EXAFS spectra for key samples are shown in Fig. 4 and compared to reference spectra for stoichiometric $UO_{2.00}$ (uncorroded uraninite) as well as $UO_{2.20}$ and $UO_{2.25}$ (U_4O_9) obtained from Conradson et al. (2005, 2004). Initial fits to the XANES data were performed using linear combinations of stoichiometric $UO_{2.0}$ and crystalline uranyl nitrate. This model assumes that all higher-valent U is present in the samples exclusively as UO_2^{2+}, for which the formal uranium oxidation state is +VI and has the specific transdioxo uranyl cation structure. This model is not appropriate for samples containing UO_{2+x}, where the predominant U site local structure is believed to be more similar to that in $UO_{2.0}$, and the oxidation state is likely to vary between +IV and +V, and possibly even as high as +VI (*vide infra*). In particular, we note that a UO_2/uranyl XANES fitting model may not detect even moderate concentrations of higher-valent uranium such as U^{V+}, particularly if it occupies a uranium lattice site in UO_{2+x}, due to the possible similarity between the XANES for U^{VI+} and U^{V+} on the same site. Therefore, in the case where UO_{2+x} is likely to be important, the most appropriate XANES model spectra are those for $UO_{2.0}$ and $UO_{2.25}$ (U_4O_9), which are likely end-members to be encountered under groundwater conditions. XANES fits to all samples, except that from the 21% P_{O2} SBR experiment, yielded 100% UO_2 regardless of the XANES model used, implying that the average uranium oxidation in the bulk of the samples was +IV within the detection limit of 5–10% $UO_{2.25}$ or uranyl. Fits to the 21% P_{O2} SBR sample, believed to be UO_{2+x} (*vide infra*) yielded 80 ± 10% $UO_{2.25}$ and the balance $UO_{2.00}$ (Fig. 4a), yielding an overall bulk stoichiometry of $UO_{2.20\pm0.025}$.

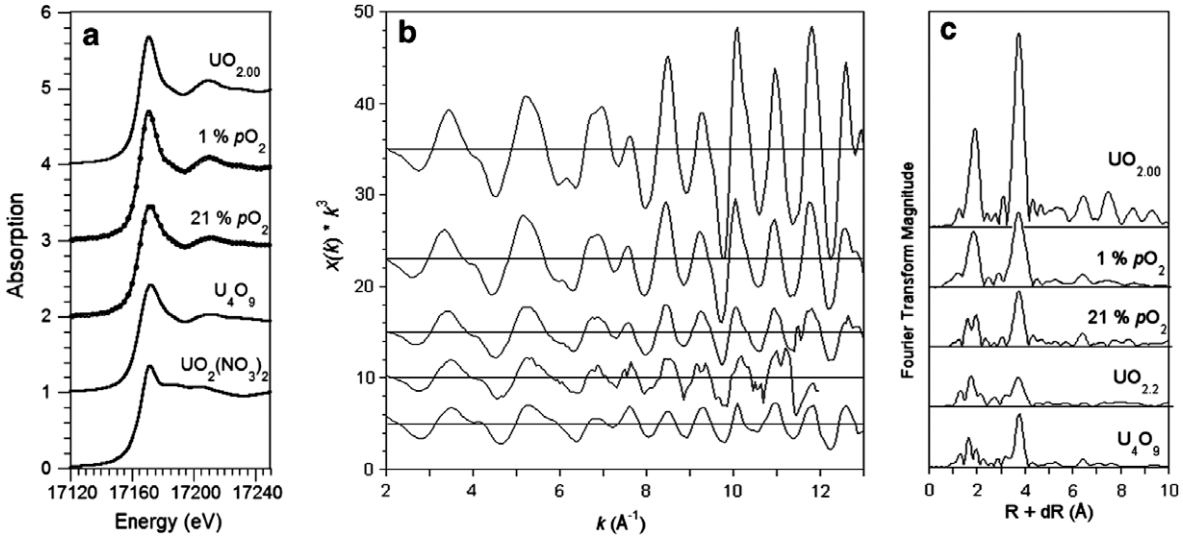

Fig. 4. (a) Uranium L_3 edge XANES spectra, (b) k^3 weighted EXAFS spectra and (c) corresponding Fourier transform magnitude of unreacted, stoichiometric $UO_{2.00}$ (serving as U(IV) reference), syn-UO_2 residue after treatment in a CFR under moderately oxidizing conditions (1% P_{O2}), syn-UO_2 residue after treatment in a SBR under strongly oxidizing conditions (21% P_{O2}), and standards of $UO_{2.20}$ (plot b and c), U_4O_9, and crystalline uranyl(VI) nitrate ($UO_2(NO_3)_2$, plot a). Solid lines represent experimental data, dotted lines show the fits.

As shown in Fig. 4, the EXAFS spectra and corresponding Fourier transforms for the 1% P_{O2} CFR sample are qualitatively similar to that of stoichiometric $UO_{2.0}$. Both show characteristic FT peaks for the shell of oxygen neighbors at 2.35 Å and next-nearest U neighbors at 3.87 Å (corresponding to FT peaks at *ca* 1.8 and 3.8 Å, R + dR, respectively). Some differences are apparent between the spectra. In particular, the relative height of the 3.8 Å U-peak is reduced as compared to that of bulk UO_2, and the FT peaks above 5 Å (R + dR), which indicate the extent of intermediate-range order in the material, are attenuated or lost. These observations indicate that, after dissolution, the average uranium environment in the samples has become disordered as compared to unreacted $UO_{2.0}$.

The EXAFS spectrum for the 21% P_{O2} SBR sample differs considerably from that of $UO_{2.0}$ and the 1% P_{O2} CFR sample. In particular, the FT peak corresponding to the 2.35 Å O-shell is sharply diminished. Moreover, there is no O-peak present at *ca* 1.5 Å (R + dR), which would be characteristic of uranyl. From these observations it can be concluded that dissolution in air-equilibrated water results in substantial disordering of the local coordination environment around U but without significant accumulation of uranyl (UO_2^{2+}). If uranyl was present, then it represented less than *ca* 10% of the total. The specific modification of the spectrum observed here is characteristic of conversion of $UO_{2.0}$ to UO_{2+x} (Conradson et al., 2004). As shown in Fig. 4, the 21% P_{O2} SBR spectrum is similar to that of $UO_{2.20}$ (the average composition as determined by XANES) and even more similar to that of U_4O_9. These observations indicate that dissolution in air-equilibrated water has resulted in the conversion of $UO_{2.0}$ to UO_{2+x}, with a composition of the final material between $UO_{2.20}$ and $UO_{2.25}$ as suggested by XANES and EXAFS combined.

Conradson et al. (2004) suggested that UO_{2+x} may contain small quantities of uranyl (up to *ca* 15% of total U in $UO_{2.20}$ and U_4O_9) as part of a separate phase exsolved within the UO_2 matrix. If uranyl were present in this form in the samples, then it would occur at or below the detection limit of the present qualitative EXAFS interpretation. To investigate the presence and role of higher valence states of uranium, XPS measurements were performed, as described in the next section.

3.4.2. X-ray photoelectron spectroscopy

The original unreacted syn-UO_2 material was analyzed by XPS to determine the near-surface stoichiometry and test whether the surface was oxidized. Several lines of evidence suggest that the surfaces of this material were not oxidized within the detection limit of XPS (~5% U(VI) or U(V), Fig. 5a). First, the FWHM values of the primary peaks (i.e., U4$f_{7/2}$ at 380.16 eV for C1s at 285.0 eV) are among the lowest reported in the literature, where the FWHM of U4$f_{7/2}$ is 1.43 eV. Despite excellent energy resolution, the primary peaks are largely symmetrical with no detectable shoulders or inflection points. The primary peak envelopes required a second small peak at slightly higher binding energy to optimize the final fit. Nonetheless, this slight asymmetry can be attributed to manifest multiplet splitting, not a second component, as suggested by *ab initio* simulations of the U4*f* XPS spectrum for UO_2 (Ilton and Bagus, 2008). Second, the spin orbit splitting (10.8 eV), and binding energy separation (6.96 eV) between the satellites and their corresponding primary peaks are close to literature values for stoichiometric $UO_{2.00}$. This last parameter is a sensitive monitor of non-stoichiometry, as even minor oxidation can significantly decrease this separation (personal observation, ESI). Further, the satellite structures (shape, position, and intensity) are also typical of stoichiometric $UO_{2.00}$. In particular, there is no indication of the U(V) satellite that appears at about 1.5 eV above the U(IV) satellite. Finally, the spectra did not vary even after several hours of intense X-ray exposure in the XPS. This is important because U(VI) and U(V) were found to be reducible under the conditions used (Ilton et al., 2007).

The XPS result of the unreacted syn-UO_2 is consistent with EXAFS spectra, which did not show evidence of U(VI) based on the detection limit of up to 10%-mass. However, the XPS results of uncleaned original bio8-UO_2 and bio6-UO_2 materials indicated small but measurable apparent non-stoichiometry (Table 2). Some proportion of this apparent non-stoichiometry might be due to oxidized U sorbed to the biomass matrix. If so, this signal would be amplified relative to the signal originating from the nanoparticulate UO_2 due to the surface sensitivity of XPS. Indeed, XANES spectroscopy did not detect any uranyl components in the nano-biogenic UO_2 (Schofield et al., 2008), although these authors pointed out that non-uranyl forms of U^{V+} and U^{VI+} could not be ruled out. In contrast, XPS analyses of biogenic UO_2 washed with anoxic NaOH solutions recorded significant increases in the proportion of U(V) at the expense of U(IV) (Table 2). This observation suggests partial pre-oxidation near the surface of the cleaned bio-UO_2 that confounded the concomitant XPS analysis of the dissolution study. Hence, the dissolution and transformation of syn-UO_2 will be the focus of the remaining spectroscopic results and discussion.

After partial dissolution of the syn-UO_2 powder in anoxic water at near-neutral pH (2 replicates), the surface of the residual solid exhibited about 18–21% of U(V) and 7–10% of U(VI), as shown by XPS (Table 2). Similar results were found after treatment at pH 2. As there is no significant difference among these results, a representative spectrum is shown in Fig. 5b. While maintaining anoxic conditions and treating the material with a 1 mM DIC solution at pH 8.5, the proportion of U(VI) on the surface did not change significantly. Although the proportion of U(V) diminished to 14%, this difference is not significant either, given the estimated relative uncertainties of ±25–30% and ±7% for ~0.1–0.2 and ~0.7 mole fraction components, respectively. When applying moderately oxidizing conditions (1% vol P_{O2}) in the absence of DIC, the proportions of U(V) and U(VI) on the UO_2 surface increased to 28% and 17%, respectively (Fig. 5c). However, XANES spectra of the syn-UO_2 residues reacted under reducing (data not shown) and moderately oxidizing conditions (Fig. 4a) consistently showed 100% U(IV), ruling out substantial oxidation in the bulk of the reacted materials. This is corroborated by the EXAFS results.

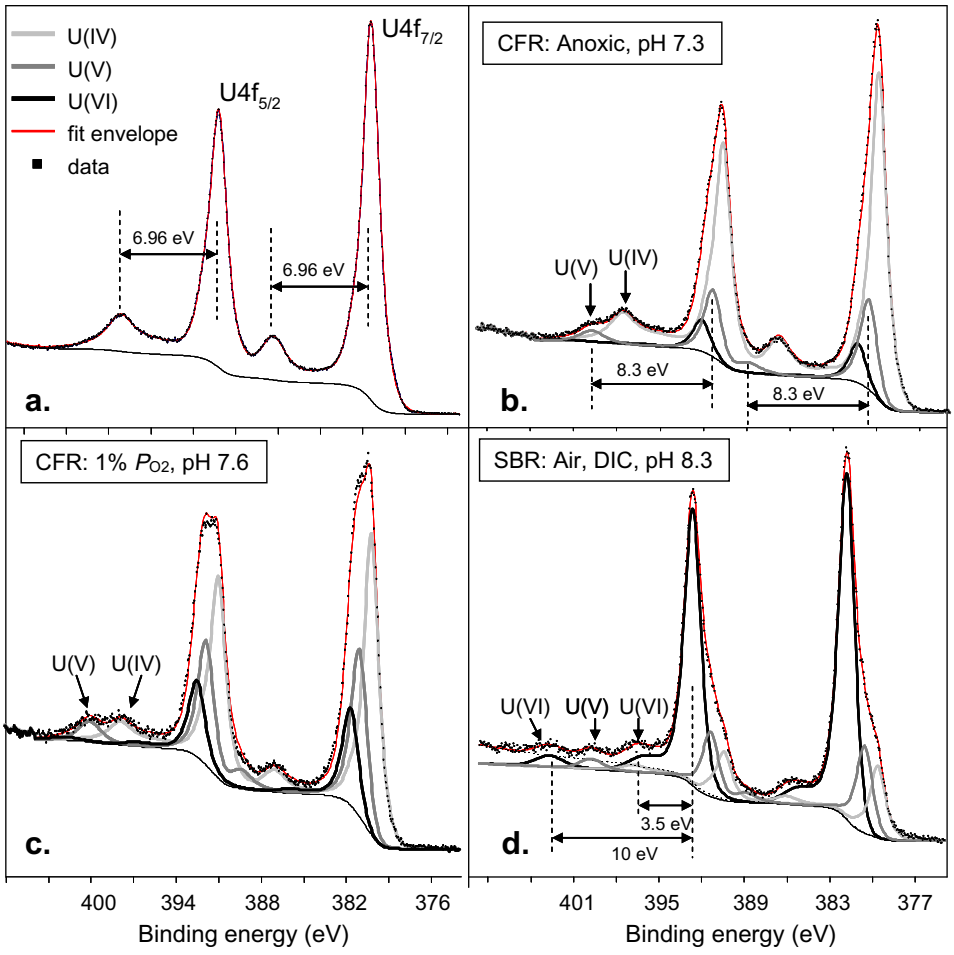

Fig. 5. Deconvolution of four representative XPS spectra of chemogenic UO_{2+x}: Original unreacted $UO_{2.0}$ material (a) and after partial dissolution in the absence of carbonate in a CFR experiment under anoxic conditions at pH 7.3 (b) and under mildly oxidizing conditions (1% P_{O2}) at pH 7.6 (c). Material from an SBR experiment carried out under strongly oxidizing conditions (air) in 1 mM DIC solution at pH 8.3 (d).

After partial dissolution of the syn-UO_2 material in air-equilibrated water (21% vol P_{O2}) containing 1 mM DIC, the XPS-detectable U(VI) fraction increased considerably to 44% in the CFR setup, and to 68% in the SBR experiment (Fig. 5d, Table 2), whereas the U(IV):U(V) ratios were close to 1 in both experiments. The EXAFS results did not support the presence of the short axial U=O bond (i.e., ~1.8 Å) typical of uranyl (V or VI), implying that the oxidized U identified by XANES primarily exists on uraninite lattice sites as charge defects. XPS results for U(V) and U(IV) yield a stoichiometry of U_4O_9. This conclusion is consistent with that obtained by XANES and EXAFS if the XPS-determined U(VI) component is restricted to the near-surface and was not measurable by XAS, whereas the UO_2 component (see Section 3.4.1.) is restricted to the particle core and was not measurable by XPS. Note that because the L-edge position for U(V) can be similar to that for U(VI), the XANES results cannot exclude U(V).

Another salient result that supports the presence of an outermost oxidized layer that was not detected by XAS is that the experiments reached saturation with respect to metaschoepite, which is consistent with the XPS-determined U4*f* binding energies of the dominant U(VI) component. Because metaschoepite, or any likely uranyl(VI) precipitate under the experimental conditions, should have the short uranyl axial bond, it is clear that EXAFS and XANES did not detect this outermost oxidized layer. Thus, as discussed later, the cumulative results are compatible with zoned particles consisting of a metaschoepite-like outer layer, a U_4O_9 intermediate layer containing 50% U(V) and 50% U(IV), and a $UO_{2.00}$ core.

The XPS analysis detected a higher proportion of U(VI) on the surface of UO_2 dissolving in the SBR compared to the material dissolving in the CFR. This result likely reflects the longer reaction time of the SBR experiment and the continuous flushing of the reactor for greater removal of U(VI) by carbonate in the CFR experiment. In contrast to the original untreated syn-UO_2 material, the near-surface of all the treated and partially dissolved materials had significant proportions of U(VI) and U(V), which further illustrates the impact of surface oxidation under both anoxic and oxic conditions and the unexpectedly high stability of a near-surface U(V) component (see Section 4.1., below).

Table 2
Percentage of U(+IV), U(+V), and U(+VI) as determined by X-ray photoelectron spectroscopy (XPS) on synthetic and biogenic UO_2 before and after continuous-flow dissolution treatments.

Sample	Treatment condition	U(+IV)	U(+V)	U(+VI)
Syn-UO_2	Original dry solid	100	0	0
Syn-UO_2	Anoxic diss, pH 7.30	75 (75)	18 (18)	7 (7)
Syn-UO_2	Anoxic diss, pH 7.31	71 (69)	20 (21)	9 (10)
Syn-UO_2	Anoxic diss, pH 2.1	76 (76)	18 (18)	6 (6)
Syn-UO_2[d]	Anoxic diss, pH 8.5, 1 mM DIC	[a]79	[a]14	[a]7
Syn-UO_2	Oxic diss, pH 7.6, 1% P_{O2}	56 (55)	28 (28)	16 (17)
Syn-UO_2	Oxic diss, pH 8.3, 1 mM DIC, Air, CFR	29 (28)	30 (28)	41 (44)
Syn-UO_2[d]	Oxic diss, pH 8.3, 1 mM DIC, Air, SBR	17 (16)	17 (16)	66 (68)
Bio6-UO_2	Original slurry, dried	88 (87)	0	12 (13)
Bio6-UO_2	1 M NaOH	49 (48)	45 (49)	6[b] (3)
Bio6-UO_2	1 M NaOH, anoxic diss, pH 7.40	39 (37)	40 (41)	21 (22)
Bio8-UO_2	Original slurry, dried	84[c] (83)	8[c] (9)	8[c] (8)
Bio8-UO_2	1 M NaOH	52 (50)	36 (36)	12 (14)
Bio8-UO_2	1 M NaOH, anoxic diss, pH 2.1	69 (67)	22 (23)	9 (10)

Values rounded off to integers. Numbers in parentheses are extrapolated time 0 values, unless otherwise noted.
[a] Sequential analyses not performed.
[b] Unexplained unusual behavior.
[c] Average value, no discernable reduction trend.
[d] Material of different production batch.

4. DISCUSSION

4.1. Mechanistic model for aqueous UO_{2+x} dissolution

Among the potential physicochemical parameters controlling uraninite dissolution in groundwater (e.g., H^+, oxidants, ligands, temperature), oxygen and carbonate are the most important variables under natural pH conditions. Extensive information is available on the corrosion of spent fuel and synthetic $UO_{2(s)}$ as a function of oxygen and carbonate concentrations (for review see Shoesmith (2000)). According to the literature, the dissolution process can be described by a three-step mechanism, (a) coordination of oxygen to the U(IV) surface followed by direct electron transfer (redox reaction), (b) surface coordination of carbonate to U(VI), and (c) detachment of a U(VI)-$CO_{3(aq)}$ species (Bruno et al., 1995; De Pablo et al., 1999). At low P_{O2}, uraninite dissolution is controlled by sorption of oxygen to the surface and thus is expected to be independent of the carbonate concentration. At high P_{O2}, carbonate coordination with U(VI) and complex detachment are expected to be rate-limiting until the [DIC] exceeds the concentration of surface bound U(VI). Both effects are reported in the literature and were consistently predicted using the general reaction model by De Pablo et al. (1999).

The present study indicates higher complexity of the UO_{2+x} dissolution processes. Dependent on the chemical conditions, the oxidative dissolution of UO_2 particles can involve an intermediate U(V) species and lead to the formation of surface layers with distinct hyperstoichiometry including $UO_{2.25}$ (U_4O_9). In synthesizing our experimental and spectroscopic results, we propose a slightly modified concept of the aqueous $UO_{2(s)}$ dissolution, the key steps of which are illustrated in Fig. 6 for reducing (Fig. 6A–C) and oxidizing conditions (Fig. 6D–F) regardless of the origin of the material (biogenic or chemogenic UO_{2+x}).

4.1.1. Reducing conditions (no DIC)

The original chemogenic $UO_{2.0}$ exhibited U(IV) both in the bulk and on the particle surface, as shown by XAS and XPS analyses. Furthermore, KPA analysis excluded dissolved U(VI) in the effluent based on a detection limit of 4.2×10^{-10} M. Although the oxidation state remains uncertain for a fraction of 10–15% of the dissolved uranium, the ICP-MS results suggest a predominance of $U(IV)_{aq}$. Hence, the main dissolution reaction for materials in contact with anoxic water at near-neutral pH is U(IV) hydrolysis (Eq. (7)), a conclusion that is consistent with the proton-promoted mechanism driving UO_{2+x} dissolution under acidic conditions (Ulrich et al., 2008).

Despite the lack of detectable U(VI) in solution, XPS recorded 7–10% U(VI) and ~20% U(V) near the syn-UO_2 surface after being suspended in anoxic, DIC-free water (Fig. 5b). The occurrence of U(V) and trace amounts of U(VI) on the chemogenic UO_2 suggests partial surface oxidation even under the reducing conditions in the experiments. The presence of U(V) on UO_2 is of particular interest because, to the best of our knowledge, it has not been reported in previous laboratory-based corrosion studies of synthetic $UO_{2(s)}$. However, a series of papers on the anodic dissolution of SIMFUEL (uranium dioxide doped with trivalent rare earth elements to increase the electronic conductivity), where the surface state of the UO_2 electrode was monitored with XPS, have reported U(V) for a wide range of solution compositions and applied potentials (Santos et al., 2004, 2006). This raises the possibility that desorption of surface bound U(V) could be contributing to the U concentrations determined by ICP-MS; any $U(V)_{aq}$ present at such low concentrations might be stable with respect to disproportionation. It further raises the possibility that $UO_{2(s)}$ solubility in water might be affected by $U(V)_{aq}$ resulting from surface oxidation of U(IV) under anoxic conditions.

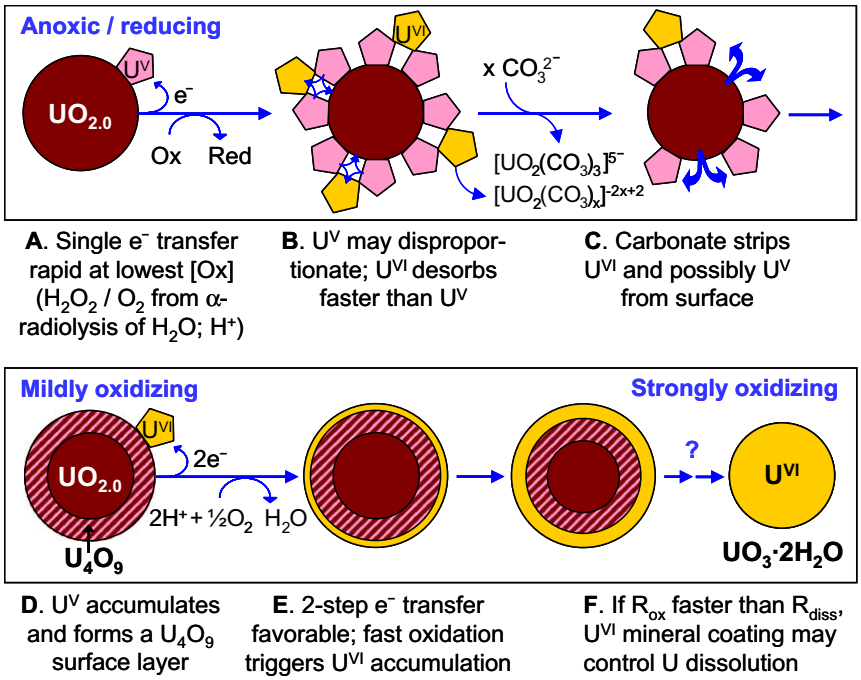

Fig. 6. Conceptual model of mechanisms of UO_2 dissolution. Balls and pentagons represent particles and ions attached to the surface, respectively. Details are explained in the text.

4.1.2. Origin of oxidants under reducing conditions

Water and its dissociation and radiolysis products can act as oxidants of UO_2. For natural uranium, water radiolysis is mainly caused by alpha radiation from ^{238}U and ^{234}U (each ~49% of activity). While the most important oxidants are H_2O_2 and O_2, H^+, HO_2^- and free radicals can also be relevant (Clarens et al., 2005; Eriksen et al., 1995). A comprehensive list of reaction pathways and products is given elsewhere (Christensen, 1998; Christensen et al., 1994).

The yield of α-radiolytic H_2O_2 generated in a CFR loaded with nanoparticulate $^{238}UO_2$ can be estimated from the specific activity of the isotope ^{238}U (12,445 Bq/g). Assuming that there is no attenuation of α-radiation within submicron particles, the radiation dose will be independent of the surface area. Given the alpha activity of 1 g of $^{238}UO_2$ (6.58×10^5 dpm, disintegrations per minute), the alpha particle energy of 5.5×10^6 eV and a product yield of 0.00985 H_2O_2 molecules per eV in neutral water (Eriksen et al., 1995), and assuming a 40 μm radius for the energy range of an emitted alpha particle in water (Kubatko et al., 2003) as well as conservative behavior for H_2O_2 (neither decay nor consumption), the H_2O_2 concentration in the CFR at steady-state can be calculated. Using a $UO_{2(s)}$ concentration of 1 g/L and integrating the α-activity over a residence time of 6 min, the H_2O_2 concentration would reach 3.55×10^{-13} M. Because this concentration is too low to account for the oxidation of a surface monolayer on uraninite under the experimental conditions, other oxidants are likely involved, for instance H_2O. In addition, O_2 can result from the decomposition of peroxide, the reduction of which was shown to be catalyzed by the formation of a thin surface layer of a mixed U(IV)/U(V) oxide (UO_{2+x}) until surface adsorbed U(VI) species begin to form (Goldik et al., 2004).

4.1.3. Surface oxidation under reducing conditions

Even if the concentrations of potential oxidants such as H_2O_2, O_2 or H^+ are extremely low, each molecule coming close to the UO_2 surface may transfer electrons to a U(IV) site. Thus, over time, the surface can become more and more oxidized. Interestingly, the XPS data consistently showed U(V) at a higher percentage than U(VI) on the anoxic syn-UO_2 surface. This is consistent with an oxidation mechanism that involves a relatively fast single electron transfer reaction to form U(V) (Eq. (10), Fig. 6A) followed by a slower second electron transfer to form U(VI) (Eq. (11), Fig. 6D).

$$UO_2 + H_2O \rightarrow (U^VO_2OH)_{ads} + H^+ + e^-_{(aq)} \quad (10)$$

$$[(U^VO_2OH)]_{ads} + H_2O \rightarrow [U^{VI}O_2(OH)_2]_{ads} + H^+ + e^-_{(aq)} \quad (11)$$

A similar oxidation mechanism was suggested for the anodic dissolution of SIMFUEL (Santos et al., 2004, 2006) based on the apparent coincident prominence of U(V) and OH^- in their XPS spectra, prompting the authors to hypothesize that an intermediate U(V) species was stabilized on the UO_2 surface in a hydrolyzed form (Eq. (10)).

Disproportionation of U(V) is another potential reaction pathway (Eq. (12)) that can limit the accumulation of U(V) and explain the occurrence of U(VI) on the UO_{2+x} surface under reducing conditions (Fig. 6B).

$$2(U^VO_2OH)_{ads} \rightarrow U^{IV}O_2 + [U^{VI}O_2(OH)_2]_{ads} \quad (12)$$

Depending on the concentration of $U(V)_{aq}$ in solution, rapid disproportionation of U(V) at the pH of the experiments would be expected. However, there is no firm evidence that sorbed U(V) is unstable with respect to disproportionation. Although this stability may depend on the substrate to which U(V) is sorbed, evidence from mica surfaces suggests that sorbed U(V) does not readily disproportionate (Ilton et al., 2005). Consequently, the most likely reaction pathway is sequential oxidation of U(IV) to U(V) to U(VI).

4.1.4. Effects of carbonate under reducing conditions

The continuous partial oxidation of the UO_{2+x} surface under reducing conditions is also illustrated by the way carbonate affects uranium release. According to thermodynamic data (Guillaumont et al., 2003) carbonate is a weak complexant for U(IV) and thus should not enhance UO_{2+x} dissolution under strictly reducing conditions and at the carbonate and pH levels of the experiments. However, our results showed that carbonate accelerated UO_2 dissolution. Carbonate is known as a strong complexant for actinyl ions. Its presence in a $UO_{2(s)} - H_2O$ system can accelerate the detachment of U(VI) from the UO_{2+x} surface once U(VI) has been formed, thus promoting U(IV) oxidation. Although U(V)-carbonate species are less stable than U(VI)-carbonate complexes (Guillaumont et al., 2003), they may act in a similar way and promote the oxidation of U(IV) to U(V) by facilitating the detachment of U(V) from the UO_{2+x} surface (Fig. 6C). Eq. (13) gives an example of such a surface reaction based on the aqueous U(V)-carbonate species $[UO_2(CO_3)_3]^{5-}$ that has been resolved by means of XAS (Docrat et al., 1999).

$$[U^{V}O_2(OH)]_{ads} + 3CO_3^{2-} \rightarrow [UO_2(CO_3)_3]^{5-} + OH^- \quad (13)$$

If in an anoxic flow-through system the carbonate-promoted rate of U(V) and U(VI) detachment from the UO_{2+x} surface is faster than the rate of U(IV) oxidation, then the introduction of carbonate should produce an initial $[U]_{diss}$ peak as the accumulated U(V) and U(VI) is removed. The peak would be followed by a continuous decline of $[U]_{diss}$ to a new steady-state level. This trend was observed for the syn-UO_2 when treated with anoxic 1 mM DIC solution (Fig. 2c). In the anoxic flow-through experiment in which carbonate was intermittently supplied, the effluent $[U]_{diss}$ increased while carbonate was present, but rapidly returned to the initial steady-state concentration after the initial conditions were re-established (Fig. 3A). These results illustrate that carbonate did not change the intrinsic oxidation kinetics of UO_2 (because it is not an oxidant), but rather it affected the detachment rate of U(IV) oxidation products from the UO_{2+x} surface.

4.1.5. Oxidizing conditions

The dissolution experiments and concomitant spectroscopic investigations showed a clear response to the increase in oxidant concentration. Even at a DO concentration as low as 0.4–0.6 mg/L (maintained by a P_{O2} of 0.01 bar in the headspace of the feed solution vessel), the fraction of U(V) and U(VI) near the UO_2 surface increased to 28% and 17% of total U (Table 2). Similarly, the KPA detected dissolved U(VI) in the effluent, but this fraction represented only 5–10% of the effluent $[U]_{diss}$. Because the concentration of the remaining 90–95% of $[U]_{diss}$ far exceeded the expected equilibrium concentration of $U(IV)_{aq}$, the KPA analyses suggest the presence of another uranium component in solution, likely $U(V)_{aq}$. Even stronger changes occurred when the [DO] was raised to ~9 mg/L in equilibrium with air. The proportion of near-surface U(VI) increased to 44% at the expense of U(IV) (Table 2), and U(VI) became the predominant fraction of the effluent $[U]_{diss}$ at about 80%. The dissolution rates of syn-UO_2 increased by a factor of ~10 (from 6×10^{-10} to 5×10^{-9} mol m^{-2} s^{-1}) when switching from 1% to 21% P_{O2} (Table 1). Because the DIC concentration was kept constant, the increase in dissolution rate reflects the expected strong dependency of the oxidation rate on the oxidant concentration.

When the supply of DO was stopped in the intermittent DO dissolution study (Fig. 3B), the effluent $[U]_{diss}$ did not decline. Rather, the steady-state concentration remained unchanged for about 20 residence times, although the feed solution in this intermittent experiment never contained any carbonate. This result suggests that the detachment of U(VI) and possibly U(V) was rate-limiting while DO was supplied in the absence of carbonate, leading to an accumulation of oxidized U near the UO_{2+x} surface (Fig. 6F). This observation is consistent with literature describing a decreasing hyperstoichiometry of the syn-UO_2 surface with increasing carbonate concentration under oxidizing conditions. While higher stoichiometric ratios of O:U were reported in the absence of bicarbonate ($x = 0.35$–0.38, Bruno et al. (1995), de Pablo et al. (1996)), treatment with 0.1 and 1.0 mM DIC solution yielded $x = 0.20$ (Gimenez et al., 2005), and an even lower value of $x = 0.05$ was found after the treatment of syn-UO_2 with a 10 mM DIC solution (De Pablo et al., 1996; Gimenez et al., 2005). Gimenez et al. (2005) concluded in their study that the non-stoichiometry was not due to deposition of a secondary solid phase. Torrero et al. (1997) determined an average solid surface stoichiometry of $UO_{2.25}$ at pH 8.2 as opposed to $UO_{2.0}$ at pH 5 and explained this difference by a diminishing rate of proton-promoted dissolution with increasing pH, enabling the incorporation of O^{2-} species into the UO_2 lattice. Thus, in the absence of more soluble aqueous U-carbonate species at neutral and alkaline conditions, the oxidative dissolution of UO_{2+x} will be controlled by the detachment of U(VI) and U(V) from the UO_{2+x} surface.

The highest U(VI) fraction on a syn-UO_2 surface (68% of total U) was determined by XPS in a SBR-based dissolution experiment in which syn-UO_2 was exposed to a 1 mM DIC solution open to air atmosphere. For this material, as outlined previously, the combined results of XANES, EXAFS and XPS suggest layered zones. A U(VI)-rich outer layer in which the binding energy is consistent with uranyl(VI) was identified by surface-sensitive XPS but not by XANES or EXAFS, a U_4O_9 middle layer containing U(IV) and U(V) for which both XPS and XANES are sensitive, and a core composed of $UO_{2.00}$ that is accessible to XANES but not to XPS (Fig. 6F). The lack of the transdioxo bonding structure as evidenced by EX-

AFS suggests that U(V) must not be present as the UO_2^+ cation and therefore we speculate that it can occupy UO_2 lattice sites as defects. Previous investigations have concluded that U_4O_9 contains both U(IV) and U(V) (Allen and Holmes, 1993). The clear evidence for U^{6+} from XPS on the other hand strongly supports the concept of a surface coating distinct from U_4O_9, consistent with a mineral phase like metaschoepite. The possibility that U(V) is incorporated at lattice sites, most likely within the U_4O_9 middle layer, might explain the surprisingly high stability of U(V) near the particle surface.

In conclusion, it is sufficient that all the XPS spectra are best fit with three components that are derived from well-characterized U(IV), U(V), and U(VI) standards and that these components maintain their separate and independent identities over a wide range of average oxidation states. Further investigation is needed to understand the formation and evolution of the proposed multi-layer oxidation structure.

4.2. Carbonate-promoted UO_{2+x} oxidation

Whereas several uraninite dissolution studies have been conducted under atmospheric P_{O2}, the present work investigated the effect of carbonate on the stability of bio- and chemogenic UO_2 at a moderate P_{O2} level of 1 vol% to simulate mildly oxidizing groundwater (Fig. 7; note that rates are compared as a function of $[CO_3^{2-}]$ and not [DIC]). Although the dissolution rates of bio-UO_2 were slightly higher than those of syn-UO_2 on a mass basis (Fig. 7a), they were lower when normalized to surface area except for the highest carbonate concentration tested (Fig. 7b). For both materials the dissolution rates increased with a similar slope up to roughly 5×10^{-6} M CO_3^{2-}. Beyond this concentration, the dissolution rates of bio-UO_2 kept increasing at a lower rate, while those of syn-UO_2 decreased slightly. Irrespective of whether or not this decrease is a real trend or an experimental artifact due to the sequential treatment of the material, the site density of surface-associated, carbonate-accessible U(VI) can be estimated by assuming that all sites were saturated with CO_3^{2-} when the dissolution rate reached its maximum. By multiplying $[CO_3^{2-}]$ by Avogadro's number and dividing by the product of *SSA* (6 m^2/g) and solids concentration (1 g/L), a carbonate-accessible site density of 0.5 nm^{-2} is calculated for the syn-UO_2. This number is very close to the >U(VI) site density of 0.6 nm^{-2} used in the study of De Pablo et al. (1999). For the bio-UO_2 particles, the unknown degree of aggregation and thus uncertainty in their effective surface area made it impossible to calculate a meaningful >U(VI) site density for the purpose of comparison.

The log-linear relationship between dissolution rate and $[CO_3^{2-}]$ (Fig. 7b) is consistent with the literature (De Pablo et al., 1999). Above a threshold CO_3^{2-} concentration the rate becomes independent of $[CO_3^{2-}]$. This pattern is consistent with a surface-controlled dissolution mechanism mediated by the binding of carbonate to initially oxidized >U(VI) surface sites. The dissolution of bio-UO_2 is comparable to that of syn-UO_2 in that it strongly depends on the carbonate concentration even in oxygen-limited (0.4–0.5 mg DO/L) neutral water.

Under nominally reducing conditions, carbonate is not expected to accelerate the UO_2 dissolution because carbonate is a strong complexing agent for UO_2^{2+} but not for U^{4+} under the given experimental conditions (Shoesmith, 2000). However, as discussed earlier, water radiolysis products can partially oxidize the UO_{2+x} surface and lead to the accumulation of corrosion product deposits such as $UO_{2.25}$ or $UO_{2.33}$ (Shoesmith, 2000). Although such deposits may reduce the rate of UO_{2+x} dissolution, the self-stabilization of the surface against corrosion would be counteracted by increasing carbonate concentration. The accelerating effect on UO_{2+x} dissolution was clearly demonstrated by the increase in effluent $[U]_{diss}$ upon the supply of DIC under reducing conditions (Fig. 1a–c). Another likely indicator of rapid dissolution of oxidized deposits on the UO_{2+x} surface is the transient peaks in the effluent $[U]_{diss}$ observed after switching from a lower to a higher DIC concentration in the feed solution (Fig. 2). This feature suggests continuous accumulation of U(V) and/or U(VI) on the UO_{2+x}

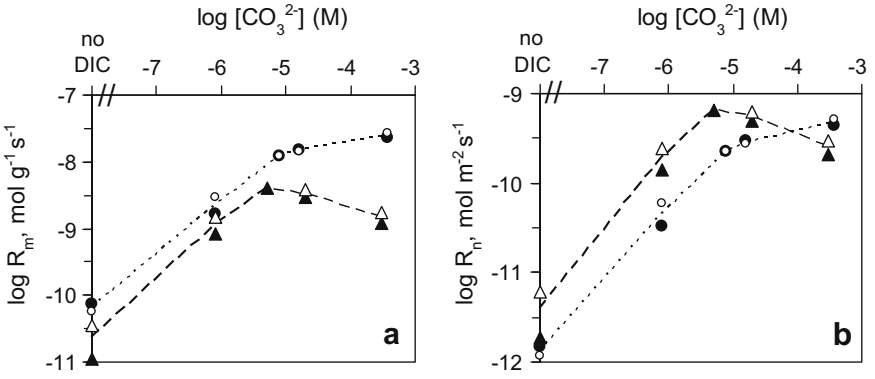

Fig. 7. Rates of UO_2 dissolution by duplicates of bio6-UO_2 (●, ○) and syn-UO_2 (▲, Δ) solids determined under moderately oxidizing conditions (1 vol% P_{O2}) as a function of CO_3^{2-} concentration. (a) Rates R_m are given per unit mass and time. (b) The surface area-normalized dissolution rates seem to become independent of carbonate at $[CO_3^{2-}] > 10^{-5}$ M, suggesting saturation of the carbonate-accessible U(VI) surface sites.

surface even during steady-state flow conditions and a fast desorption reaction when providing higher carbonate concentrations.

The average dissolution rates of syn-UO_2 from this study can be compared with previously published data. The rate obtained under a 1 vol% P_{O2} atmosphere at 0.1 mM DIC and pH 8.2 (2.0×10^{-10} mol m^{-2} s^{-1}) was similar to numbers reported for higher DIC concentrations and in the presence of air (Table 1). For example, Pierce et al. (2005) measured a rate of 1.0×10^{-10} mol m^{-2} s^{-1} for the dissolution of crystalline UO_2 at 10^{-3} M DIC and pH 8.0. A rate of 1.6×10^{-10} mol m^{-2} s^{-1} was obtained when dissolving syn-UO_2 at 10^{-2} M DIC and pH 8.5 (Bruno et al., 1995; De Pablo et al., 1996). In contrast, the dissolution rate of syn-UO_2 determined in the present study under atmospheric conditions, 1 mM DIC and pH 8.0 (4.8×10^{-9} mol m^{-2} s^{-1}) was 48-times higher than the rate published for similar conditions (Pierce et al., 2005). This discrepancy can be due to the higher flow rate and the sequential treatment of the UO_{2+x} material used in our study.

In natural groundwater, divalent earth alkali cations such as Ca^{2+} and Mg^{2+} are common constituents that can form very stable aqueous complexes with uranyl carbonate (Dong and Brooks, 2006). Hence, such species may accelerate UO_2 dissolution in a similar manner to carbonate alone, by accelerating the detachment of surface-associated oxidized uranium species. Divalent cations may also interact with U(V) carbonato complexes, but it is unknown whether such species would favor enhanced dissolution or potentially stabilize the U_4O_9 surface layer.

4.3. Comparison of bio-UO_2 and syn-UO_2 dissolution

The cleaned biogenic and the chemogenic uraninite solids exhibited similar dissolution trends and comparable rates under the experimental conditions, with one exception. Although the steady-state concentrations of dissolved uranium were generally higher for the bio-UO_2 compared to the syn-UO_2 (Figs. 1 and 2), the dissolution rates generally agreed within a factor 2–4 when normalized to the BET surface area (Table 1). Given the complexity of the dissolution experiments and the number of variables that add uncertainty to the systems (e.g., mass and homogeneity of the initial solids, analytical uncertainties, variation among replicates), differences in rates within a factor of 4 are not likely to be significant. Based on this result, within the margin of experimental uncertainty, the tested biogenic and synthetic UO_2 materials exhibited similar reactivity with respect to oxidative and carbonate-promoted dissolution, where the detachment of U(VI) and probably U(V) is the dissolution rate-limiting step. This similarity in reactivity of the two size fractions (~3 nm and 100–200 nm particles) implies that the principal surface reactions, at least the rates of oxidation and dissolution, are comparable. This in turn suggests similar types and densities of reactive surface sites und thus surface free energy. A similar conclusion was obtained with regard to Zn(II) sorption on biogenic, nanoparticulate UO_2 and bulk uraninite (Singer et al., 2009).

The exception to the trend of similar reactivity for the biogenic and chemogenic uraninites in the present study is the observation made under reducing conditions in the presence of carbonate, where the dissolution rate of bio6-UO_2 was about 20-times higher than that of syn-UO_2 (Table 1), indicating that carbonate-promoted the UO_2 dissolution more for the biogenic nanoparticles than for the chemogenic material. A plausible cause is the higher initial surface oxidation after pretreatment, in particular the accumulation of U(V) and U(VI) near the surface which may give rise to faster detachment of the oxidized uranium species. At the high pH during the NaOH treatment of the biogenic UO_2, surface oxidation can be more favorable due to higher activity of water radiolysis products and/or faster oxidation kinetics. Through protolysis of H_2O_2 the perhydroxy anion HO_2^- can form and act as an oxidant and a precursor of a chain of radicals that produce an even stronger oxidizing environment (Clarens et al., 2005). To verify the impact of the NaOH treatment, the reactivity of uncleaned bio-UO_2 material has to be determined. The presence of organic matter, in particular when associated with the bio-UO_2 surface, may lower the UO_2 reactivity and preserve the material against oxidative dissolution (Singer et al., 2009).

5. CONCLUSIONS

The long-term stability of biogenic uraninite is a seminal factor governing the success of bioremediation of uranium-contaminated sites. The stability of nanoparticulate UO_{2+x} will depend on structural properties that determine surface reactivity and on physicochemical factors that control surface reactions. Building on the recently described structural homology of biogenic nanoparticulate UO_2 obtained from *S. oneidensis* MR-1 and chemogenic $UO_{2.00}$, the goal of this study was to compare both materials with respect to their intrinsic solubility and dissolution kinetics under a variety of geochemical conditions and to investigate the dissolution mechanisms by bulk XAS and surface-sensitive XPS. The following conclusions are relevant to uranium geochemistry and bioremediation.

1. The thermodynamic solubility data accepted for so-called amorphous $UO_{2(s)}$ are suitable in predicting the intrinsic solubility of undoped biogenic UO_{2+x} nanoparticles in near-neutral water under anoxic conditions.
2. Within the margin of experimental uncertainty and when normalized to surface area, dissolution rates of bio- and chemogenic UO_{2+x} were similar under carbonate-free reducing and oxidizing conditions, respectively. This similarity enables the modeling of the thermodynamic and kinetic properties of undoped biogenic UO_{2+x} nanoparticles based on those known for chemogenic $UO_{2.00}$.
3. In near-neutral water, dissolved inorganic carbon, which is an ubiquitous groundwater component, reversibly promotes the dissolution of UO_{2+x} not only under strongly oxidizing conditions by forming highly soluble U(VI)-carbonate complexes, but also under nominally reducing conditions, where water and its radiolysis products (e.g., H_2O_2, O_2, and radicals) can serve as oxidants.

This study has shown that intermediate U(V) species can accumulate on the UO_{2+x} surface. Formation of soluble U(V)-carbonate complexes is a likely driving force for promoting UO_{2+x} dissolution under anoxic conditions.

4. The mechanism of UO_2 oxidation appears to be more complex than usually assumed. Spectroscopic and analytical data from XPS, XANES, EXAFS, and KPA combined with experimental results from the carbonate treatment of dissolving $UO_{2.0}$ support the formation of a near-surface layer with an approximate $UO_{2.25}$ stoichiometry, characterized by a 1:1 ratio of U(IV) to U(V). Whereas low oxidant concentrations lead to an intermediate surface U(V) species, the sequential electron transfer from U(IV) to U(V) to U(VI) becomes favorable under strongly oxidizing conditions.
5. At the most oxidizing conditions studied the detachment of surface U(VI) appears to be rate-limiting in the absence and presence of carbonate up to a threshold concentration above which all accessible U(VI) sites are saturated with carbonate. The accumulated U(VI) can evolve to a metaschoepite-like coating on the UO_{2+x} surface layer, passivating the $UO_{2.0}$ core by controlling the uranium solubility and dissolution kinetics. Future studies should quantify the oxidative dissolution process of layered nano-scale UO_{2+x} materials in the field and explore the environmental significance of natural dopants and U(V) intermediate species.

ACKNOWLEDGMENTS

We thank Dan Schwarz and David Clark for providing synthetic $UO_{2.00}$ material and Satya Chinni for running samples on the KPA. We are grateful to Sabine Ulrich, Edgar Leslie, and Scott Dixon for their assistance in the laboratory. We appreciate helpful discussions with Steven Conradson. We thank the Associate Editor, Dr. Zhu, and two anonymous reviewers who helped improve an earlier draft of this manuscript. Funding was provided by the U.S. Department of Energy, Office of Basic Energy Sciences grant # DE-FG02-06ER64227, through the linked Grants 1027869 (SSRL), 1027833 (EPFL), and 1027834 (WU). Part of this research was carried out at the Stanford Synchrotron Radiation Lightsource, a national user facility operated by Stanford University on behalf of the U.S. DOE-OBER. Portions of this project were supported by the DOE-BER-funded SSRL Environmental Remediation Science Program and the DOE-BER and NIH-NCRR-funded SSRL Structural Molecular Biology Program. Work carried out at EPFL was funded in part by the Swiss NSF Grant #20021-113784.

REFERENCES

Abdelouas A., Lutze W. and Nuttall H. E. (1999) Oxidative dissolution of uraninite precipitated on Navajo sandstone. *J. Cont. Hydrol.* **36**(3–4), 353–375.

Allen G. C. and Holmes N. R. (1993) Mixed-valency behavior in some uranium-oxides studies by x-ray photoelectron spectroscopy. *Can. J. Appl. Spectrosc.* **38**(5), 124–130.

Belai N., Frisch M., Ilton E. S., Ravel B. and Cahill C. L. (2008) Pentavalent uranium oxide via reduction of $[UO_2]^{2+}$ under hydrothermal reaction conditions. *Inorg. Chem.* **47**(21), 10135–10140.

Brooks S. C., Fredrickson J. K., Carroll S. L., Kennedy D. W., Zachara J. M., Plymale A. E., Kelly S. D., Kemner K. M. and Fendorf S. (2003) Inhibition of bacterial U(VI) reduction by calcium. *Environ. Sci. Technol.* **37**(9), 1850–1858.

Bruno J., Casas I., Cera E., De Pablo J., Gimenez J. and Torrero M. E. (1995) Uranium (IV) dioxide and SIMFUEL as chemical analogues of nuclear spent fuel matrix dissolution. A comparison of dissolution results in a standard $NaCl/NaHCO_3$ solution. *Scientific Basis for Nuclear Waste Management XVII. Symposium*, vol. 1. pp. 601–608.

Burgos W. D., McDonough J. T., Senko J. M., Zhang G. X., Dohnalkova A. C., Kelly S. D., Gorby Y. and Kemner K. M. (2008) Characterization of uraninite nanoparticles produced by *Shewanella oneidensis* MR-1. *Geochim. Cosmochim. Acta* **72**(20), 4901–4915.

Casas I., Gimenez J., Marti V., Torrero M. E. and Depablo J. (1994) Kinetic studies of unirradiated UO_2 dissolution under oxidizing conditions in batch and flow experiments. *Radiochim. Acta* **66–67**, 23–27.

Chinni S., Anderson C., Ulrich K.-U., Giammar D. E. and Tebo B. M. (2008) Indirect UO_2 oxidation by Mn(II)-oxidizing spores of *Bacillus* sp. strain SG-1 and the effect of U and Mn concentrations. *Environ. Sci. Technol.* **42**(23), 8709–8714.

Christensen H. (1998) Calculations simulating spent-fuel leaching experiments. *Nucl. Technol.* **124**(2), 165–174.

Christensen H., Sunder S. and Shoesmith D. W. (1994) Oxidation of nuclear fuel (UO_2) by the products of water radiolysis: development of a kinetic model. *J. Alloys Comp.* **213**(214), 93–99.

Clarens F., de Pablo J., Casas I., Gimenez J., Rovira M., Merino J., Cera E., Bruno J., Quinones J. and Martinez-Esparza A. (2005) The oxidative dissolution of unirradiated UO_2 by hydrogen peroxide as a function of pH. *J. Nucl. Mater.* **345**(2–3), 225–231.

Conradson S. D., Begg B. D., Clark D. L., den Auwer C., Ding M., Dorhout P. K., Espinosa-Faller F. J., Gordon P. L., Haire R. G., Hess N. J., Hess R. F., Keogh D. W., Lander G. H., Manara D., Morales L. A., Neu M. P., Paviet-Hartmann P., Rebizant J., Rondinella V. V., Runde W., Tait C. D., Veirs D. K., Villella P. M. and Wastin F. (2005) Charge distribution and local structure and speciation in the UO_{2+x} and PuO_{2+x} binary oxides for $x \leqslant 0.25$. *J. Solid State Chem.* **178**(2), 521–535.

Conradson S. D., Manara D., Wastin F., Clark D. L., Lander G. H., Morales L. A., Rebizant J. and Rondinella V. V. (2004) Local structure and charge distribution in the UO_2–U_4O_9 system. *Inorg. Chem.* **43**(22), 6922–6935.

de Pablo J., Casas I., Gimenez J., Marti V. and Torrero M. E. (1996) Solid surface evolution model to predict uranium release from unirradiated UO_2 and nuclear spent fuel dissolution under oxidizing conditions. *J. Nucl. Mater.* **232**(2–3), 138–145.

de Pablo J., Casas I., Gimenez J., Molera M., Rovira M., Duro L. and Bruno J. (1999) The oxidative dissolution mechanism of uranium dioxide. I. The effect of temperature in hydrogen carbonate medium. *Geochim. Cosmochim. Acta* **63**(19/20), 3097–3103.

Docrat T. I., Mosselmans J. F. W., Charnock J. M., Whiteley M. W., Collison D., Livens F. R., Jones C. and Edmiston M. J. (1999) X-ray absorption spectroscopy of tricarbonatodioxouranate(V), $[UO_2(CO_3)_3]^{5-}$, in aqueous solution. *Inorg. Chem.* **38**(8), 1879–1882.

Dong W. M. and Brooks S. C. (2006) Determination of the formation constants of ternary complexes of uranyl and carbonate with alkaline earth metals (Mg^{2+}, Ca^{2+}, Sr^{2+}, and Ba^{2+}) using anion exchange method. *Environ. Sci. Technol.* **40**(15), 4689–4695.

Eriksen T. E., Eklund U. B., Werme L. and Bruno J. (1995) Dissolution of irradiated fuel: a radiolytic mass balance study. *J. Nucl. Mater.* **227**(1–2), 76–82.

Finch R. J. and Ewing R. C. (1992) The corrosion of uraninite under oxidizing conditions. *J. Nucl. Mater.* **190**, 133–156.

Finneran K. T., Housewright M. E. and Lovley D. R. (2002) Multiple influences of nitrate on uranium solubility during bioremediation of uranium-contaminated subsurface sediments. *Environ. Microbiol.* **4**(9), 510–516.

Frazier S. W., Kretzschmar R. and Kraemer S. M. (2005) Bacterial siderophores promote dissolution of UO_2 under reducing conditions. *Environ. Sci. Technol.* **39**(15), 5709–5715.

Fredrickson J. K., Zachara J. M., Kennedy D. W., Liu C. X., Duff M. C., Hunter D. B. and Dohnalkova A. (2002) Influence of Mn oxides on the reduction of uranium(VI) by the metal-reducing bacterium *Shewanella putrefaciens*. *Geochim. Cosmochim. Acta* **66**(18), 3247–3262.

Fredrickson J. K., Zachara J. M., Marshall M. J. and Beliaev A. S. (2007) Biogeochemical mechanisms controlling reduced radionuclide particle properties and stability. In *2nd Annual DOE-ERSP PI Meeting: Abstracts. LBNL-59453 Abs. 2007*, Lawrence Berkeley National Laboratory, p. 44.

Gimenez J., Clarens F., Casas I., Rovira M., de Pablo J. and Bruno J. (2005) Oxidation and dissolution of UO_2 in bicarbonate media: implications for the spent nuclear fuel oxidative dissolution mechanism. *J. Nucl. Mater.* **345**(2–3), 232–238.

Ginder-Vogel M., Criddle C. S. and Fendorf S. (2006) Thermodynamic constraints on the oxidation of biogenic UO_2 by Fe(III) (hydr)oxides. *Environ. Sci. Technol.* **40**(11), 3544–3550.

Goldik J. S., Nesbitt H. W., Noel J. J. and Shoesmith D. W. (2004) Surface electrochemistry of UO_2 in dilute alkaline hydrogen peroxide solutions. *Electrochim. Acta* **49**(11), 1699–1709.

Gorby Y. A. and Lovley D. R. (1992) Enzymic uranium precipitation. *Environ. Sci. Technol.* **26**(1), 205–207.

Gu B. H., Yan H., Zhou P., Watson D. B., Park M. and Istok J. (2005) Natural humics impact uranium bioreduction and oxidation. *Environ. Sci. Technol.* **39**(14), 5268–5275.

Guillaumont R., Fanghänel T., Fuger J., Grenthe I., Neck V., Palmer D. A. and Rand M. H. (2003) *Update on the chemical thermodynamics of uranium, neptunium, plutonium, americium and technetium*. Elsevier.

Ilton E. S. and Bagus P. S. (2008) Ligand field effects on the multiplet structure of the U4f XPS of UO_2. *Surf. Sci.* **602**(5), 1114–1121.

Ilton E. S., Boily J. F. and Bagus P. S. (2007) Beam induced reduction of U(VI) during X-ray photoelectron spectroscopy: the utility of the U4f satellite structure for identifying uranium oxidation states in mixed valence uranium oxides. *Surf. Sci.* **601**(4), 908–916.

Ilton E. S., Haiduc A., Cahill C. L. and Felmy A. R. (2005) Mica surfaces stabilize pentavalent uranium. *Inorg. Chem.* **44**(9), 2986–2988.

Ilton E. S., Haiduc A., Moses C. O., Heald S. M., Elbert D. C. and Veblen D. R. (2004) Heterogeneous reduction of uranyl by micas: crystal chemical and solution controls. *Geochim. Cosmochim. Acta* **68**(11), 2417–2435.

Janeczek J. and Ewing R. C. (1992a) Dissolution and alteration of uraninite under reducing conditions. *J. Nucl. Mater.* **190**, 157–173.

Janeczek J. and Ewing R. C. (1992b) Structural formula of uraninite. *J. Nucl. Mater.* **190**, 128–132.

Jang J. H., Dempsey B. A. and Burgos W. D. (2006) Solubility of schoepite: comparison and selection of complexation constants for U(VI). *Water Res.* **40**(14), 2738–2746.

Kraemer S. M. and Hering J. G. (1997) Influence of solution saturation state on the kinetics of ligand-controlled dissolution of oxide phases. *Geochim. Cosmochim. Acta* **61**(14), 2855–2866.

Kubatko K. A. H., Helean K. B., Navrotsky A. and Burns P. C. (2003) Stability of peroxide-containing uranyl minerals. *Science* **302**(5648), 1191–1193.

Langmuir D. (1978) Uranium solution-mineral equilibria at low temperatures with applications to sedimentary ore deposits. *Geochim. Cosmochim. Acta* **42**(6, Part 1), 547–569.

Lasaga A. C., Soler J. M., Ganor J., Burch T. E. and Nagy K. L. (1994) Chemical-weathering rate laws and global geochemical cycles. *Geochim. Cosmochim. Acta* **58**(10), 2361–2386.

Lovley D. R. and Phillips E. J. P. (1992) Bioremediation of uranium contamination with enzymatic uranium reduction. *Environ. Sci. Technol.* **26**(11), 2228–2234.

Lovley D. R., Phillips E. J. P., Gorby Y. A. and Landa E. R. (1991) Microbial reduction of uranium. *Nature* **350**, 413–416.

Moon H. S., Komlos J. and Jaffe P. R. (2007) Uranium reoxidation in previously bioreduced sediment by dissolved oxygen and nitrate. *Environ. Sci. Technol.* **41**(13), 4587–4592.

N'Guessan A. L., Vrionis H. A., Resch C. T., Long P. E. and Lovley D. R. (2008) Sustained removal of uranium from contaminated groundwater following stimulation of dissimilatory metal reduction. *Environ. Sci. Technol.* **42**(8), 2999–3004.

Pierce E. M., Icenhower J. P., Serne R. J. and Catalano J. G. (2005) Experimental determination of UO_2(cr) dissolution kinetics: effects of solution saturation state and pH. *J. Nucl. Mater.* **345**(2–3), 206–218.

Rehr J. J., Albers R. C. and Zabinsky S. I. (1992) High-order multiple-scattering calculations of X-ray absorption fine structure. *Phys. Rev. Lett.* **69**(23), 3397–3400.

Renshaw J. C., Lloyd J. R. and Livens F. R. (2007) Microbial interactions with actinides and long-lived fission products. *Comptes Rendus Chimie* **10**(10–11), 1067–1077.

Santos B. G., Nesbitt H. W., Noel J. J. and Shoesmith D. W. (2004) X-ray photoelectron spectroscopy study of anodically oxidized SIMFUEL surfaces. *Electrochim. Acta* **49**(11), 1863–1873.

Santos B. G., Noel J. J. and Shoesmith D. W. (2006) The effect of pH on the anodic dissolution of SIMFUEL (UO_2). *J. Electroanal. Chem.* **586**(1), 1–11.

Schecher W. D. and McAvoy D. C. (1998) MINEQL+: a chemical equilibrium modeling system, version 4.5. Environmental Research Software.

Schofield E. J., Veeramani H., Sharp J. O., Suvorova E., Bernier-Latmani R., Mehta A., Stahlman J., Webb S. M., Clark D. L., Conradson S. D., Ilton E. S. and Bargar J. R. (2008) Structure of biogenic uraninite produced by *Shewanella oneidensis* strain MR-1. *Environ. Sci. Technol.* **42**(21), 7898–7904.

Senko J. M., Istok J. D., Suflita J. M. and Krumholz L. R. (2002) In-situ evidence for uranium immobilization and remobilization. *Environ. Sci. Technol.* **36**(7), 1491–1496.

Senko J. M., Kelly S. D., Dohnalkova A. C., McDonough J. T., Kemner K. M. and Burgos W. D. (2007) The effect of U(VI) bioreduction kinetics on subsequent reoxidation of biogenic U(IV). *Geochim. Cosmochim. Acta* **71**(19), 4644–4654.

Senko J. M., Mohamed Y., Dewers T. A. and Krumholz L. R. (2005a) Role for Fe(III) minerals in nitrate-dependent microbial U(IV) oxidation. *Environ. Sci. Technol.* **39**(8), 2529–2536.

Senko J. M., Suflita J. M. and Krumholz L. R. (2005b) Geochemical controls on microbial nitrate-dependent U(IV) oxidation. *Geomicrobiol. J.* **22**(7–8), 371–378.

Shoesmith D. W. (2000) Fuel corrosion processes under waste disposal conditions. *J. Nucl. Mater.* **282**, 1–31.

Singer D. M., Farges F. and Brown G. E. (2007) Biogenic UO_2 – characterization and surface reactivity. *Am. Inst. Phys. Conf. Proc. 13th Int XAFS Conf.* **882**(1), 277–279.

Singer D. M., Farges F. and Brown, Jr., G. E. (2009) Biogenic nanoparticulate UO_2: synthesis, characterization, and factors affecting surface reactivity. *Geochim. Cosmochim. Acta* **73**(12), 3593–3611.

Suzuki Y. and Suko T. (2006) Geomicrobiological factors that control uranium mobility in the environment: update on recent advances in the bioremediation of uranium-contaminated sites. *J. Miner. Petrol. Sci.* **101**(6), 299–307.

Thomas G. F. and Till G. (1984) The dissolution of unirradiated UO_2 fuel pellets under simulated disposal conditions. *Nucl. Chem. Waste Manage.* **5**(2), 141–147.

Torrero M. E., Baraj E., De Pablo J., Gimenez J. and Casas I. (1997) Kinetics of corrosion and dissolution of uranium dioxide as a function of pH. *Int. J. Chem. Kinet.* **29**(4), 261–267.

Ulrich K. U., Singh A., Schofield E. J., Bargar J. R., Veeramani H., Sharp J. O., Bernier-Latmani R. and Giammar D. E. (2008) Dissolution of biogenic and synthetic UO_2 under varied reducing conditions. *Environ. Sci. Technol.* **42**(15), 5600–5606.

Wall J. D. and Krumholz L. R. (2006) Uranium reduction. *Annu. Rev. Microbiol.* **60**, 149–166.

Wan J. M., Tokunaga T. K., Brodie E., Wang Z. M., Zheng Z. P., Herman D., Hazen T. C., Firestone M. K. and Sutton S. R. (2005) Reoxidation of bioreduced uranium under reducing conditions. *Environ. Sci. Technol.* **39**(16), 6162–6169.

Webb S. M. (2005) SIXPack: a graphical user interface for XAS analysis using IFEFFIT. *Phys. Scripta* **T115**, 1011–1014.

Wu W. M., Carley J., Luo J., Ginder-Vogel M. A., Cardenas E., Leigh M. B., Hwang C. C., Kelly S. D., Ruan C. M., Wu L. Y., Van Nostrand J., Gentry T., Lowe K., Mehlhorn T., Carroll S., Luo W. S., Fields M. W., Gu B. H., Watson D., Kemner K. M., Marsh T., Tiedje J., Zhou J. Z., Fendorf S., Kitanidis P. K., Jardine P. M. and Criddle C. S. (2007) In situ bioreduction of uranium (VI) to submicromolar levels and reoxidation by dissolved oxygen. *Environ. Sci. Technol.* **41**(16), 5716–5723.

Zhong L. R., Liu C. X., Zachara J. M., Kennedy D. W., Szecsody J. E. and Wood B. (2005) Oxidative remobilization of biogenic uranium(IV) precipitates: effects of iron(II) and pH. *J. Environ. Qual.* **34**(5), 1763–1771.

Zhou P. and Gu B. H. (2005) Extraction of oxidized and reduced forms of uranium from contaminated soils: effects of carbonate concentration and pH. *Environ. Sci. Technol.* **39**(12), 4435–4440.

Associate editor: Chen Zhu